



Article

The emplacement, alteration, subduction and metamorphism of metagranites from the Tso Morari Complex, Ladakh Himalaya

Anna K. Bidgood^{1*} , David J. Waters^{2,3} , Brendan J. Dyck⁴  and Nick M.W. Roberts⁵ 

¹Irish Centre for Research in Applied Geosciences, O'Brien Centre for Science (East), University College Dublin, Belfield, Dublin 4, Ireland; ²Department of Earth Sciences, University of Oxford, OX1 3AN, UK; ³Museum of Natural History, University of Oxford, OX1 3PW, UK; ⁴Department of Earth, Environmental and Geographical Sciences, University of British Columbia, Kelowna, V1V 1V7, Canada; and ⁵Geochronology and Tracers Facility, British Geological Survey, Keyworth, Nottingham, UK, NG12 5GG

Abstract

Eclogite-facies mineral assemblages are commonly preserved in mafic protoliths within continental terranes. It is widely accepted that the entirety of these continental terrains must also have been subducted to eclogite-facies conditions. However, evidence that the felsic material transformed at eclogite-facies conditions is lacking. Low-strain metagranites of the ultrahigh-pressure metamorphic Tso Morari Complex in Ladakh, Himalaya, are host to eclogite-facies mafic sills and preserve evidence of subduction to eclogite-facies conditions. Following the eclogite-facies metamorphism, the granites and their gneissic equivalents were overprinted by amphibolite-facies Barrovian metamorphism, obscuring their earlier metamorphic history. We present evidence that the Tso Morari metagranites preserve a complex magmatic, hydrothermal and polymetamorphic history that involved four stages. Stage 1 was magmatic crystallisation, a record of which is preserved in the primary igneous mineralogy and relict igneous microstructures. Monazite grains record a U–Pb age of 474.0 ± 11.6 Ma, concurrent with a published zircon crystallisation age. Stage 2 represents pervasive late-magmatic hydrothermal alteration of the granite during emplacement and is evident in the mineral composition, particularly in the white micas preserved in the igneous domains. Stage 3 involved the (ultra)high-pressure metamorphism of these granite bodies during the Himalayan subduction of continental material. The high-pressure stage of the metamorphic history (>25 kbar at 550 – 650°C) is preserved as thin coronas of garnet and phengite around igneous biotite, garnet with kyanite inclusions in pseudomorphs after cordierite, and rare palisade quartz textures after coesite. Stage 4 was a result of Barrovian metamorphism of the Tso Morari Complex and is evident in the replacement of garnet by biotite. Many of these features are preserved in localised textural domains in the rock, where local equilibrium was important and the anhydrous conditions limited reaction progress, though aided preservation potential. Collectively, these four stages record a 480 Myr history of metamorphism and reworking of the northernmost Indian plate.

Keywords: granite, textures, hydrothermal, metamorphism, continental subduction, exhumation, alteration, Tso Morari, Himalaya

(Received 4 February 2022; accepted 24 October 2022; Accepted Manuscript published online: 16 November 2022; Associate Editor: Thomas Mueller)

Introduction

In continental high-pressure metamorphic terranes, it is commonly observed that quartzofeldspathic rocks such as granites, gneisses and metasedimentary rocks, which host eclogite-facies mafic rocks, record lower-pressure amphibolite-facies conditions (e.g. Chopin, 1984; Smith, 1984; Young and Kylander-Clark, 2015). The discovery of minor ultrahigh-pressure (UHP) mafic rocks within lower pressure felsic terranes led to an early debate as to whether the whole tectonic unit experienced the same conditions or whether the mafic eclogites were introduced tectonically (Lappin, 1977; Smith, 1980; Cuthbert and Carswell, 1982). The observation that, in some cases, the host quartzofeldspathic

rocks also preserve some transformation at eclogite-facies conditions led to the understanding that the eclogites were metamorphosed *in situ*, and that water availability, residence time at depth, bulk composition and deformation were all factors that influence the equilibration of felsic rocks under eclogite-facies pressures (e.g. Austrheim, 1986; Koons *et al.*, 1987; Rubie, 1990; Cuthbert *et al.*, 2000; Wain *et al.*, 2000). Debate continues as to whether the pre-existing mineral assemblages in quartzofeldspathic rocks persist metastably throughout their high-pressure metamorphic evolution, or are transformed and retrogressed pervasively leaving little record of high-pressure mineral assemblages (e.g. Wain *et al.*, 2001; Young and Kylander-Clark, 2015).

The occurrence and timing of mineral transformations during continental subduction is relevant to geophysical models that either neglect phase transitions, or assume complete transformation over large volumes. Transformation of felsic rocks during subduction influences the density and strength of crustal material and is therefore a key component related to the exhumation of

*Author for correspondence: Anna K. Bidgood, Email: akbidgood@gmail.com

Cite this article: Bidgood A.K., Waters D.J., Dyck B.J. and Roberts N.M.W. (2023) The emplacement, alteration, subduction and metamorphism of metagranites from the Tso Morari Complex, Ladakh Himalaya. *Mineralogical Magazine* 87, 40–59. <https://doi.org/10.1180/mgm.2022.121>

UHP material from depth (Warren, 2013). Incomplete transformation at eclogite-facies conditions may be a common feature in 'dry' felsic rocks, allowing strong metastable crust to persist during subduction (e.g. Peterman *et al.*, 2009; Krabbendam *et al.*, 2000; Wain *et al.*, 2001).

Zones of low strain at regional and outcrop scales provide a unique window into the early tectonic history of metamorphic rocks in these high-pressure terranes and can preserve an extensive and protracted history (e.g. Krabbendam and Wain, 1997; Wain *et al.*, 2001). Eclogite bodies, granulite-facies intermediate-mafic metaplutonic rocks (Krabbendam and Wain, 1997) and meta-granitoids (Biino and Compagnoni, 1992; Gebauer *et al.*, 1997; Koons *et al.*, 1987) occur as low-strain enclaves preserving eclogite-facies mineral assemblages within pervasively deformed gneisses in terranes such as the Bergen Arcs (Austrheim and Griffin, 1985) and Western Gneiss Region of Norway (Mørk, 1985; Austrheim and Engvik, 1997); the Sulu orogen (Hirajima *et al.*, 1993; Wallis *et al.*, 2007; Zhang and Liou, 1997), the Sesia Zone (Oberhänsli *et al.*, 1985) and Dora Maira massif (Koons *et al.*, 1987; Biino and Compagnoni, 1992) in the European Alps; and the Tso Morari Complex (Sachan *et al.*, 2004) and Kaghan valley (Pognante and Spencer, 1991) in the Himalaya.

This investigation describes the microstructure, mineral composition, timing and conditions of the metamorphic evolution of a suite of low-strain metagranites from the Tso Morari Complex, an ultrahigh-pressure metamorphic dome in Ladakh, NW Himalaya (Fig. 1). Whereas eclogite-facies metamorphism has been recorded in mafic bodies, very little evidence has survived in the volumetrically dominant amphibolite-facies felsic rocks. The peak pressure estimates of 26–42 kbar in this complex (de Sigoyer *et al.*, 1997; Guillot *et al.*, 1997; St-Onge *et al.*, 2013; Chatterjee and Jagoutz, 2015; Wilke *et al.*, 2015) lie within the coesite stability field, and were first confirmed by the discovery of coesite preserved in an eclogite boudin (Sachan *et al.*, 2004). However, evidence of ultrahigh-pressure metamorphism in the felsic rocks of the Tso Morari Complex has been documented only as pseudomorphs after coesite in a low-strain metagranite (Bidgood *et al.*, 2021). Accompanying high-pressure metamorphic reactions have not been previously recorded in the host Puga gneiss, owing to the pervasive amphibolite-facies overprint.

The Tso Morari metagranites form metre- to kilometre-scale zones of low strain within the high-strain amphibolite-facies Puga Gneiss, which is itself of broadly granitic composition. They preserve evidence of a history of emplacement, alteration and metamorphism that spans c. 480 Myr. Observations of mineral textures and compositions in the granite are interpreted as a record of magmatic and magmatic–hydrothermal processes, overprinted by high-pressure metamorphism, and ultimately followed by Barrovian metamorphism with attendant regional deformation. Many of these early features are preserved in discrete textural domains in the rock, where local equilibrium was important, with dry conditions limiting reaction progress and aiding preservation potential.

Geological setting

The Tso Morari dome (Fig. 1) is composed of a set of stacked nappes, forming a doubly-plunging northwest–southeast elongate dome, with the stratigraphically lowest units cropping out in the centre of the dome (Steck *et al.*, 1998). The lowermost nappe is known as the Tso Morari Complex and contains Ordovician

granite intruded into Cambrian sediments atop the Indian plate. The dominant lithology within the complex is the Puga Gneiss. Low-strain granitic domains are present throughout the complex, ranging in size from approximately one metre in diameter to map-scale domains that are over a square kilometre in area, such as in the Polokongka La region, where large boulders litter the glacial landscape, and Nuruchen, southwest of Tso Kar. The Polokongka La granite is a coarse-grained peraluminous S-type granite with an $Al_2O_3/(CaO+Na_2O+K_2O)$ ratio in the range 0.88–1.98 (Girard and Bussy, 1999). Early investigators mapped the Polokongka La granite as a discrete body, presumed intrusive to the Puga Gneiss (Thakur and Virdi, 1979; Fuchs and Linner, 1996; Guillot *et al.*, 1997). However, Girard and Bussy (1999) and Epard and Steck (2008) emphasised the lack of observed intrusive relationships, the heterogeneous deformation, and the continuous transition between low-strain granite and gneiss. Near identical zircon morphology and U–Pb ages (Girard and Bussy, 1999) suggest that these lithologies actually belong to the same intrusive package and represent relatively low- and high-strain versions.

Both the Tso Morari metagranite and the deformed Puga Gneiss host mafic eclogite boudins, which indicates that the entirety of the Tso Morari Complex experienced eclogite-facies metamorphism (de Sigoyer *et al.*, 1997; Guillot *et al.*, 1997; Sachan *et al.*, 2004). However, there is currently little reported evidence, other than prograde garnet zoning (Bidgood, 2020) and quartz textures after coesite (Bidgood *et al.*, 2021), that the Puga Gneiss and granitoids underwent mineralogical transformation to eclogite-facies assemblages. The majority of the Tso Morari complex contains regional amphibolite facies Barrovian assemblages (Epard and Steck, 2008; St-Onge *et al.*, 2013; Palin *et al.*, 2014).

Analytical methods

Scanning electron microscopy

Back-scattered electron imaging of textures and semi-quantitative maps of corona and pseudomorphic textures were collected from carbon coated thin sections using an FEI Quanta 650 FEG E-Scanning electron microscope at the University of Oxford, equipped with an energy dispersive spectrometer (EDS). Maps were acquired with an accelerating voltage of 15 kV using Oxford Instruments AZtec (version 3.3) acquisition software.

Electron probe microanalysis

Thin sections were made from 11 samples from the Tso Morari metagranites (Table 1). Samples TMG01, 02, 06 and 11 were selected for detailed petrological analysis. Major-element compositions of minerals that exhibit solid solutions were measured using a Cameca SX-5 field emission electron probe microanalyser (EPMA) at the Department of Earth Sciences, University of Oxford. All EPMA were conducted with 15 kV acceleration potential and 20 nA beam current. For all major elements, the on-peak count time was 30 s with 30 s of background collection. Titanium was measured with a 60 s on-peak count time and 60 s of background collection. A range of natural and synthetic oxide standards were used including: albite (Na, Al, Si); MgO (Mg); wollastonite (Ca); andradite (Fe); Mn metal (Mn); and TiO₂ (Ti), and analyses were verified against secondary mineral standards. Raw analyses were automatically corrected for atomic

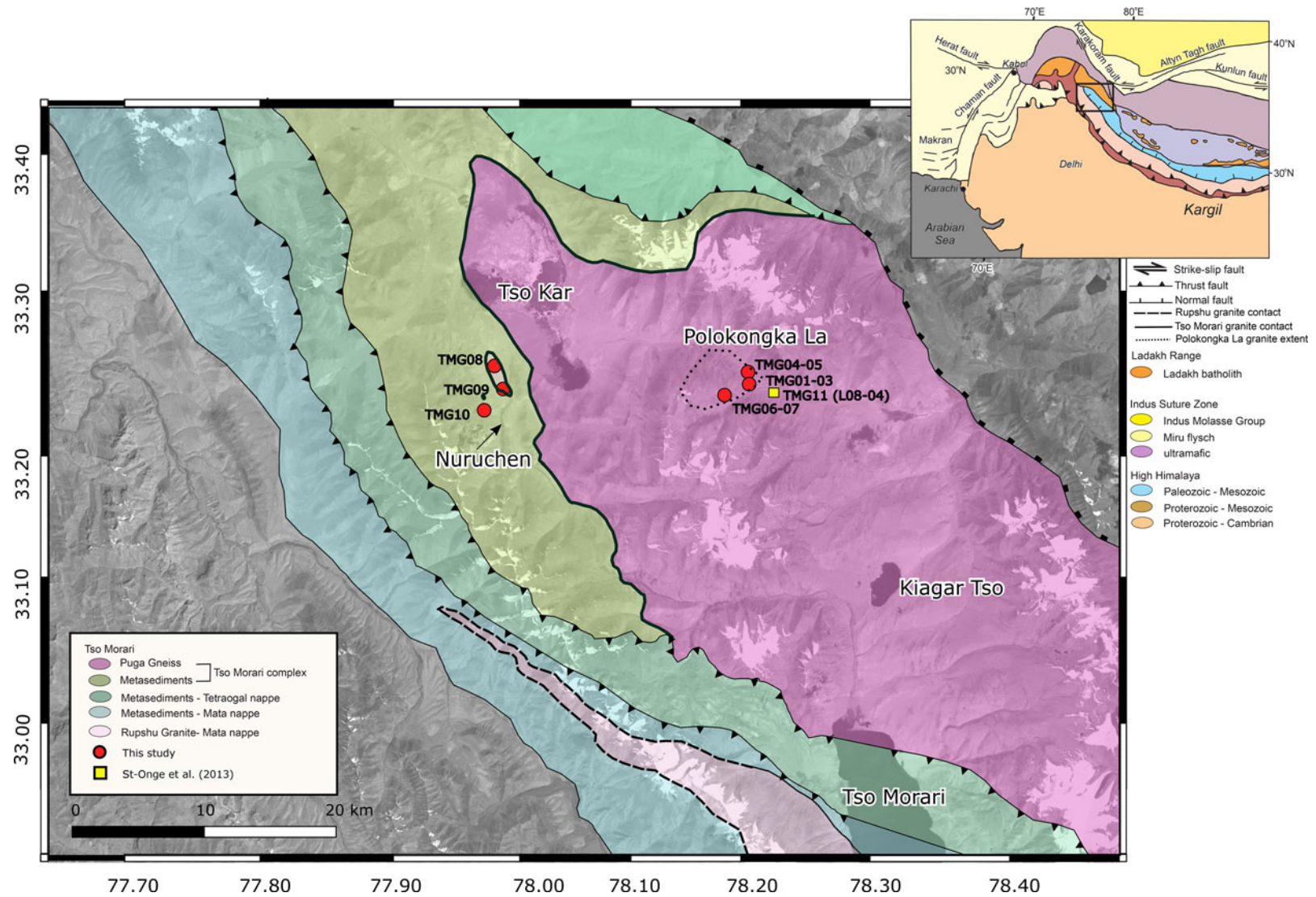


Fig. 1. Geological map adapted from Epard and Steck (2008), St-Onge *et al.* (2013) and references therein, showing the location of geochronological samples. The approximate location of Polokongka La granite outcrops and boulder field are outlined with a black dashed line. Red dots show locations of low-strain granite samples collected by Anna Bidgood in 2016 and 2017 field seasons. The yellow square shows the approximate location of a low-strain granite sample within the Polokongka La granite region, collected in 2008 by Mike Searle and featured in St-Onge *et al.* (2013). Background USGS Landsat data downloaded from <https://earthexplorer.usgs.gov/>. Colouring corresponds to bands 762, greyscale by luminosity.

Table 1. Sample locations, rock type, assemblage and domains present. A description of different domains can be found in the text. Sample name is as referred to in field notebooks.

Sample number	Sample name	Coordinates (°)	Location	Rock type	Outcrop	Assemblage*	Domains
TMG01	11-01	33.235N, 78.369E	Rulung valley	Cordierite granite	boulder	Kfs, Qz, Ab, Bt, Ms/Ph, Grt, Ky, Ilm, Rt, Ap, Zrn, Mnz	1,2,3,4,5
TMG02	11-02	33.235N, 78.369E	Rulung valley	K-feldspar megacryst	boulder	Kfs, Qz, Ms/Ph, Bt, Ab, Grt, Ilm, Ap, Zrn	1,2,3,4
TMG03	11-02c	33.235N, 78.369E	Rulung valley	Cordierite-Qtz enclave	boulder	Kfs, Qz, Ab, Bt, Ms/Ph, Grt, Ky, Ilm, Rt, Ap, Zrn, Mnz	1,2,4,5
TMG04	a05-01	33.24N, 78.241E	Polokongka La	Granite	outcrop	Kfs, Qz, Ms/Ph, Bt, Ab, Grt, Ilm, Ep, Ap, Zrn	1,2,3,4
TMG05	a05-02	33.24N, 78.241E	Polokongka La	Granite	outcrop	Kfs, Qz, Ms/Ph, Bt, Ab, Grt, Ilm, Ep, Ap, Zrn	1,2,3,4
TMG06	a05-10	33.246N, 78.188E	Polokongka La ridge	Grt-granite	boulder	Kfs, Qz, Ms/Ph, Bt, Ab, Grt, Ilm, Ap, Zrn	1,2,3,4
TMG07	a05-17	33.246N, 78.188E	Polokongka La ridge	Granite	outcrop	Kfs, Qz, Ms/Ph, Bt, Ab, Ilm, Ep, Ap, Zrn	1,2,3,4
TMG08	a10-06	33.24601N, 77.98E	Nuruchen	Granite	outcrop	Kfs, Qz, Ab, Ms/Ph, Bt, Grt, Ky, Ilm, Ap, Zrn, Mnz	1,2,3,4,5
TMG09	a10-07	33.24601N, 77.98E	Nuruchen	Granite	outcrop	Kfs, Qz, Ab, Ms/Ph, Bt, Grt, Ky, Ilm, Ap, Zrn,	1,2,3,4,5
TMG10	a12-01	33.232N, 77.989E	Nuruchen	Granite	outcrop	Kfs, Qz, Ab, Ms/Ph, Bt, Grt, Ilm, Ap, Zrn,	1,2,3,4,5
TMG11	L08-04	unknown	Polokongka La	Granite	unknown	Kfs, Qz, Ab, Ms/Ph, Bt, Czo, Ilm, Ap, Zrn	1,2,3,4

*Mineral abbreviations mostly according to Warr (2021): Ab = albite; Ap = apatite; Bt = biotite; Czo = Clinozoisite; Ep = epidote; Grt = garnet; Ilm = ilmenite; Kfs = K-feldspar; Ky = kyanite; Mnz = monazite; Ms/Ph = muscovite/phenigite; Qz = quartz; Rt = rutile; and Zrn = zircon.

number, absorption and fluorescence using the $\phi\rho z$ matrix correction routine (Merlet, 1994). Mineral spot analyses and line profiles were taken across micas and garnet to determine the extent of intracrystalline compositional variation. Representative compositions are in Table 2, and a full list is in the Supplementary materials.

Laser ablation mass spectrometry

Monazite grains were imaged using back-scattered electron imaging to identify any zoning present using the FEI Quanta 650 FEG E-Scanning electron microscope (E-SEM) at the University of Oxford. The U–Pb age of monazite was measured *in situ* using a Nu Instruments Atom single-collector inductively coupled plasma mass spectrometer (SC-ICP-MS) at the Geochronology and Tracers Facility, British Geological Survey, using the method described in Mottram *et al.* (2014). Analytical conditions and results are provided in Supplementary tables. Laser parameters were a static spot of 12 μm diameter, ablated for 30 s, at a repetition of 10 Hz, with a fluence of 2.5 J/cm^2 . The primary reference material used was Stern monazite (Palin *et al.*, 2013; Horstwood *et al.*, 2016), and secondary reference materials Manangotry monazite (Paquette *et al.*, 1994; Palin *et al.*, 2013; Horstwood *et al.*, 2016) and 44069 (Aleinikoff *et al.*, 2006; Buick *et al.*, 2011). Data reduction used an in-house spreadsheet for normalisation and *IsoplotR* (Vermeesch, 2018) for plotting and age calculation. Uncertainty propagation follows Horstwood *et al.* (2016), with the final age quoted as $\pm \alpha/\beta$, where α does not propagate systematic uncertainties, and β does. The secondary reference materials gave weighted mean $^{206}\text{Pb}/^{238}\text{U}$ ages of 553.0 ± 5.6 Ma (Manangotry) and 430.8 ± 4.3 Ma (44069), which are within 1.5% of the accepted ages.

Phase equilibrium modelling

Constraints on the pressure–temperature evolution of sample TMG01 were determined by scanning a representative area within a garnet + mica domain using the SEM-EDS system described above. The integrated bulk composition in weight % oxides, normalised to 100% anhydrous (Table 3), is SiO_2 45.26; TiO_2 0.20; Al_2O_3 30.93; FeO 12.75; MnO 0.48; MgO 3.53; CaO 0.12; Na_2O 0.33; and K_2O 6.40. H_2O was set in excess, to fully saturate all assemblages in the investigated P–T space. The phase equilibrium model was calculated in the ten-component system MnO – Na_2O –

CaO – K_2O – FeO – MgO – Al_2O_3 – SiO_2 – H_2O – TiO_2 (MnNCKFMASHT) using *Theriak/Domino* v.2015 with thermodynamic dataset ds55 (Holland and Powell, 1998; updated August 2004), adapted by Doug Tinkham. The following activity composition models were used: Holland and Powell (2003) for ternary plagioclase and K-feldspar; White *et al.* (2007) for garnet with added spessartine and biotite with added mnbi phase component from the software list; Mahar *et al.* (1997) and Holland and Powell (1998) for chlorite with added mnchl phase component, as in Tinkham *et al.* (2001); Coggon and Holland (2002) for white mica with their pyrophyllite and margarite members excluded due to the consistent overestimation of the stability of these end-members; White *et al.* (2000, 2005) for ilmenite (Mn system); and Holland and Powell (1998) for epidote. The following pure phases that are not part of a converted solution model were added: H_2O , quartz, kyanite, albite, rutile and sphene (titanite).

Description and composition of textural domains

The Tso Morari metagranites are coarse-grained porphyritic granitic rocks that consist of quartz, alkali feldspar, white mica, biotite and albite \pm garnet with accessory apatite, zircon, monazite and rutile with ilmenite rims. During deformation of the complex, the major part of the granitic protolith developed a pervasive fabric, forming the Puga Gneiss, which is dominated by assemblages of mica, albite and quartz, with less abundant K-feldspar. Quartz- and mica-rich folia wrap K-feldspar augen. The state of strain is variable, but is commonly highest towards the margins of eclogite dykes and boudins, where the gneiss may also contain abundant garnet.

Primary igneous minerals and textures are best preserved in the low-strain metagranites together with evidence for mineral reactions at different stages of its evolution, allowing a more comprehensive understanding of the geological history of the complex to be decoded. The Tso Morari metagranites contain coarse-grained phenocrysts of inclusion-rich K-feldspar reaching up to 15 mm in length, with a matrix grain size of 5 mm. The coarse-grained minerals, as seen in thin section (Fig. 2a) or in hand specimen (Fig. 2g), are best characterised as mineral domains that retain relict igneous textures. The metagranites also contain numerous enclaves, with a rounded shape and diffuse margins, reaching up to 50 cm in diameter. Although compositionally distinct, they contain mineral domains closely comparable to those in the porphyritic metagranite. The most common type consists

Table 2. Representative compositions for mineral phases in the Tso Morari granites.*

Domain	Kfs + white mica			White mica + Ab (Pl)			Micaceous domains (Bt, Ms)			
	A	B	C	A	B	C	A	B	C	D
Mineral	Kfs	coarse white mica	fine white mica	Pl	albite	white mica	coarse Bt	Bt aggregate	coarse white mica	white mica after Bt
Sample Number	11-01 TMG01	L08-04 TMG11	L08-04 TMG11	11-01 TMG01	11-02 TMG02	11-02 TMG02	L08-04 TMG11	a05-10 TMG06	L08-04 TMG11	11-01 TMG01
SiO ₂	64.36	46.58	50.08	62.10	68.07	48.63	33.26	37.31	45.72	47.01
TiO ₂	0.06	0.16	0.14	–	0.07	0.01	2.06	2.68	0.09	0.52
Al ₂ O ₃	18.86	37.90	27.00	23.30	20.65	35.60	18.17	16.16	37.45	33.36
FeO	0.01	1.14	4.17	–	–	1.85	25.14	20.79	1.27	2.26
MnO	0.01	0.05	0.06	–	–	0.01	0.30	0.06	0.02	0.01
MgO	–	0.50	2.34	0.01	–	0.85	4.44	9.10	0.56	1.26
CaO	–	–	0.09	4.68	0.48	0.12	0.03	0.06	–	0.02
Na ₂ O	0.93	0.24	0.06	8.94	9.86	0.70	0.06	0.13	0.59	0.20
K ₂ O	15.04	10.19	10.93	0.13	0.05	10.20	9.20	9.00	10.52	9.44
Total	99.27	96.76	94.87	99.13	99.18	97.97	92.67	95.29	96.22	94.08
Oxygens	8	22	22	8	8	22	22	22	22	22
Si	2.98	6.06	6.79	2.77	2.98	6.28	5.37	5.69	6.02	6.31
Ti	–	0.02	0.01	–	0.00	0.00	0.25	0.31	0.01	0.05
Al	1.03	5.82	4.32	1.23	1.06	5.42	3.46	2.91	5.81	5.28
Fe	0.00	0.12	0.47	–	–	0.20	3.40	2.65	0.14	0.25
Mn	0.00	0.01	0.01	–	–	0.00	0.04	0.01	0.00	0.00
Mg	–	0.10	0.47	0.00	–	0.16	1.07	2.07	0.11	0.25
Ca	–	–	0.01	0.22	0.02	0.02	0.01	0.01	–	0.00
Na	0.08	0.06	0.01	0.77	0.84	0.18	0.02	0.04	0.15	0.05
K	0.89	1.69	1.89	0.01	0.00	1.68	1.90	1.75	1.76	1.62
Sum	4.99	13.88	13.98	5.00	4.91	13.94	15.52	15.44	14.00	13.83

Domain	Grt + mica (Crd)									
	E	F	G	H	A	B	C	D	E	
Mineral	Grt corona	coarse Grt	Bt after Grt	white mica inclusions in Grt	coarse white mica	coarse Bt	Grt	fine white mica	Bt after Grt	
Sample Number	11-01 TMG01	a05-10 TMG06	11-02 TMG02	a05-10 TMG06	11-01 TMG01	11-02 TMG02	11-01 TMG01	11-01 TMG01	11-01 TMG01	
SiO ₂	36.72	37.85	38.47	48.55	46.33	37.23	37.94	49.98	36.57	
TiO ₂	0.10	0.06	0.09	0.19	0.02	0.02	–	–	0.02	
Al ₂ O ₃	21.02	22.15	17.51	35.53	33.61	18.09	21.57	32.74	18.82	
FeO	32.31	31.83	20.08	1.49	1.93	21.21	32.11	1.40	16.79	
MnO	1.32	0.15	0.21	0.02	0.01	0.22	1.00	0.13	0.12	
MgO	1.59	2.28	9.72	0.59	1.80	9.33	6.23	2.03	11.86	
CaO	5.13	6.69	–	0.07	0.03	0.02	0.10	0.09	0.06	
Na ₂ O	0.03	–	0.07	0.67	0.17	0.09	0.02	0.23	0.07	
K ₂ O	0.05	–	9.65	8.66	10.87	9.35	0.01	9.80	8.98	
Total	98.27	101.05	95.80	95.77	94.78	95.56	98.98	96.40	93.28	
Oxygens	12	12	22	22	22	22	12	22	22	
Si	3.00	2.98	5.81	6.33	6.23	5.67	3.01	6.52	5.58	
Ti	0.01	0.00	0.01	0.02	0.00	0.00	–	–	0.00	
Al	2.02	2.06	3.12	5.46	5.33	3.25	2.02	5.03	3.39	
Fe	2.21	2.10	2.54	0.16	0.22	2.70	2.13	0.15	2.14	
Mn	0.09	0.01	0.03	0.00	0.00	0.03	0.07	0.02	0.02	
Mg	0.19	0.27	2.19	0.12	0.36	2.12	0.74	0.39	2.70	
Ca	0.45	0.56	–	0.01	0.00	0.00	0.01	0.01	0.01	
Na	0.00	–	0.02	0.17	0.04	0.03	0.00	0.06	0.02	
K	0.01	–	1.86	1.44	1.87	1.82	0.00	1.63	1.75	
Sum	7.98	7.98	15.58	13.71	14.06	15.62	7.98	13.81	15.61	

*Abbreviations – Ab = albite; Bt = biotite; Crd = cordierite; Grt = garnet; Kfs = K-feldspar; Ms = Muscovite; and Pl = plagioclase. ‘–’ = not detected.

of domain 1 (quartz, Fig. 2b) and domain 5 (garnet + mica, Fig. 2f).

There are five textural domains common to all of the granitic samples investigated (Fig. 2b–f). These are described below, in non-genetic terms.

Quartz-rich domains

The quartz-rich domain consists of both individual and clusters of bipyramidal quartz grains that are ~3–4 mm in diameter.

Most quartz-rich domains display undulose extinction and/or fine deformation lamellae (Fig. 2b). Quartz clusters are made up of idiomorphic crystals that are typically joined along prism and rhombohedral facets (Fig. 3a). Both the clustered quartz grains and individual idiomorphic grains are surrounded by other mineral/textural domains of similar size, retaining primary igneous relationships with these domains (Fig. 2a,b).

Single crystals of quartz exhibit low-strain internal features such as subgrain formation and incipient recrystallisation, which is commonly confined to grain boundaries (Fig. 3b).

Table 3. Composition of garnet + mica domain 5 taken from the representative element map from Sample TMG01.

Oxide wt.%		Cations pfu (18 oxygens)		Normalised to 5 Si
SiO ₂	45.26	Si	4.90	5.00
TiO ₂	0.20	Ti	0.02	0.02
Al ₂ O ₃	30.93	Al	3.95	4.03
FeO	12.75	Fe	1.15	1.18
MnO	0.48	Mn	0.04	0.04
MgO	3.53	Mg	0.57	0.58
CaO	0.12	Ca	0.01	0.01
Na ₂ O	0.33	Na	0.07	0.07
K ₂ O	6.40	K	0.88	0.90
Total	100.00	Cation sum	11.59	11.84
		Alkali sum		0.98

Chessboard subgrains (~0.5 mm in diameter) are present within some of these grains (Fig. 3c). Locally, smaller subgrains have developed on a scale of <0.1 mm within the chessboard subgrains (Fig. 3c). Quartz grain boundaries are commonly gently lobate at a scale of ~0.1 mm as a result of minor grain-boundary migration (Fig. 3d,e). In contrast to the single quartz crystals preserved in all of the samples investigated from the Tso Moriri Complex quartz domains in sample TMG06 from the Polokongka La region preserve palisade microstructures (Fig. 3f).

K-feldspar + white mica domains

The K-feldspar + white mica domains form the largest domains (up to 15 cm in length in outcrop) and are commonly observed to enclose the other four domain types (Fig. 2c, 4a–d). These domains commonly contain a single large K-feldspar megacryst (Or₉₃), with microcline twinning and fine string and bleb perthitic microtextures, that has undergone near-pervasive sericitisation (Fig. 2a and 4a). Fine-grained white mica forms micaceous patches within the K feldspar (Fig. 4c) which plot along the celadonite exchange vector, with increasing Si and Mg per formula unit (pfu) (Fig. 5a), and the main cluster ranges from 6.5 to 6.9 Si pfu. The K-feldspar + white mica domains also contain coarse-grained white micas replacing K-feldspar, ~0.5–1 mm in length (Fig. 2c, Fig. 4b–d) with a low phengite and high paragonite content (Fig. 5a–c). A finer-grained recrystallised rim of the coarser generation (Fig. 4b–d, 5d,f) has Si pfu > 6.7 (Fig. 5a–c).

Certain areas within K-feldspar phenocrysts represent inclusions of other minerals. Commonly these are rectangular areas in which albite is intergrown with a fine-grained white mica (Fig. 4a). This mica is texturally distinct from the even finer grained sericite-like mica that forms irregular patches after K-feldspar (Fig. 4c). These areas strongly resemble the white mica + albite domains described in the following section, although they are smaller in size.

White mica + albite domains

The third type of domain is the white mica + albite domain which consists of a fine-grained aggregate of white mica and albite that, under plane polarised light, appears darker than the K-feldspar + white mica domain and commonly exhibits zoning between dark core regions and pale rims (Fig. 2d, 4e–f). The composition of the white mica plots along the celadonite exchange vector with > 6.5 Si pfu (Fig. 5a). In some samples (e.g. TMG11) radial clusters of

clinozoisite needles occur in turbid regions within this domain (Fig. 4f). In less-altered samples (e.g. TMG01), islands of plagioclase are also present with an anorthite content of 12–25 mol.%, preserved among micaceous alteration.

Micaceous domains

The micaceous domains vary in character across the samples. In the least altered samples (e.g. TMG01), this domain forms rectangular regions, commonly occupied by a large single mica crystal of muscovite or biotite (Fig. 2e, 6b, c). In other samples, the micaceous domains manifest as polycrystalline clusters of biotite and white mica. Coarse-grained muscovite in the micaceous domains has the lowest phengite and highest paragonite content of the white micas (Fig. 5a–c), comparable to coarse-grained white micas in the K-feldspar + white mica domains (Fig. 5d–f). The rims of these coarse-grained micas have recrystallised to form fine-grained phengitic white mica.

The coarse grained biotites are compositionally homogeneous with a dark brown-red colour and a Ti content of 0.25–0.38 pfu and $X_{Mg} = Mg/(Mg + Fe)$ of 0.21–0.39 (Fig. 6b). Geometrical arrays of rutile needles form a sagenitic texture (c.f. Shau *et al.*, 1991) parallel to the cleavage planes (Fig. 6c). Trails of densely packed zircon inclusions and apatite crosscut the cleavage of the grains. The coarse-grained biotites have reaction coronas ~30 µm wide (Fig. 6a–c) consisting of phengite (6.6–6.8 Si pfu) intergrown with fingers of ilmenite, surrounded by a continuous corona of granular garnet. The garnet coronas preserve a range of compositions from Alm₈₇Py₆Grs₂Sps₅ to Alm₅₅Py₃Grs₄₀Sps₂ with a pronounced gradient in grossular content from 2 mol.% in contact with the biotite to 40 mol.% in contact with albite. In some instances, the white mica + ilmenite and garnet coronas are surrounded by a second rim of white mica with a higher phengite content of 6.9–7.1 Si pfu.

In some samples, coarse-grained biotites are replaced by aggregates of abundant red-brown fine-grained biotite (Fig. 6e–f) which form distinct, non-rectangular regions surrounded by thin rims of white mica and ilmenite (e.g. samples TMG06, 08 and 09). The boundaries of the micaceous aggregates are commonly defined by small (~0.5 mm) idioblastic garnets with distinct core and rim zones (Fig. 6f). In sample TMG06, large garnet crystals completely replace coarse red biotite domains and have a rim of brown biotite (Fig. 6d, e).

Garnet + mica domains

The garnet + mica domains have well-defined boundaries and are essentially composed of fine-grained white mica with small irregular clusters of garnet and kyanite (Fig. 7a–e). Coarse aggregates of white mica and biotite have occasionally grown perpendicular to the domain boundaries (Fig. 2f). Biotite is generally colourless, with lower Ti and higher Mg ($X_{Mg} = 0.41–0.55$) than observed in Ti-rich biotites of the micaceous domain. Coarse-grained white micas have a phengite content of c. 6.2 Si pfu which correlates closely with the lower phengite content of the coarse-grained white mica in both the micaceous domains and the K feldspar + white mica domains.

Small garnets (0.1 mm) contain randomly oriented kyanite needles and have notably grossular-poor compositions of Alm_{72–79}Py_{20–26}Grs_{0.06–0.2}Sps_{1.3–2.5}. Garnets may be partially- or completely-replaced by fine-grained brown biotite (Fig. 7f) with a low Ti content (0.09 pfu) and a relatively high X_{Mg} of 0.46–

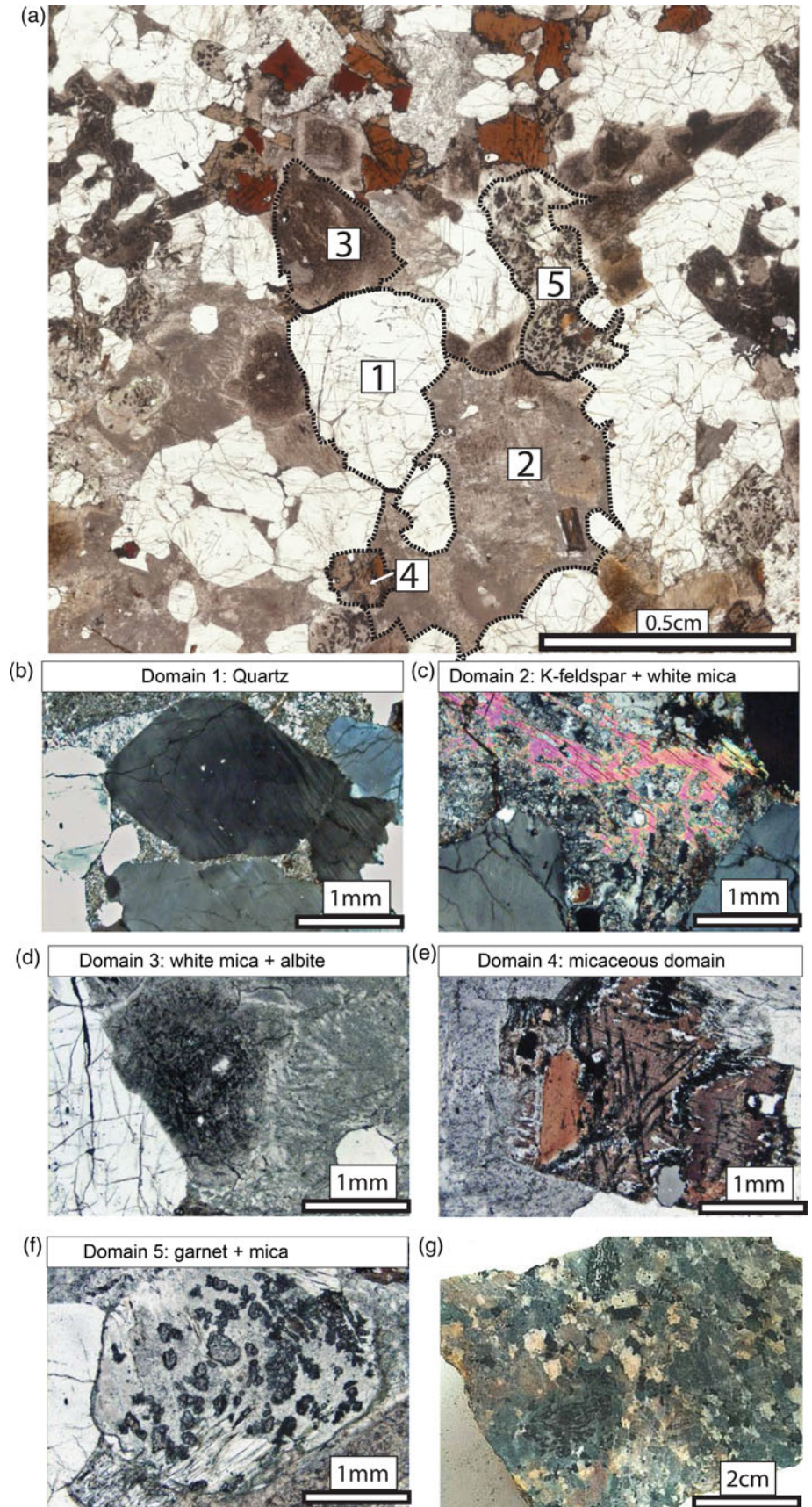


Fig 2. (a) Sample TMG01 (scanned thin section) showing the location of representative domains with igneous textural relationships, as referred to in the text. (b) Quartz-rich domain 1, crossed-polars image of euhedral quartz with strain lamellae. (c) K-feldspar + white mica domain 2, crossed polars. (d) White mica + albite (domain 3), plane-polarised light (PPL). (e) Micaceous domain 4, PPL image of euhedral biotite partially replaced by ilmenite and muscovite following the older sagenitic texture. (f) White mica + garnet domain 5, PPL. (g) Sample TMG10 cut hand specimen showing granitic texture.

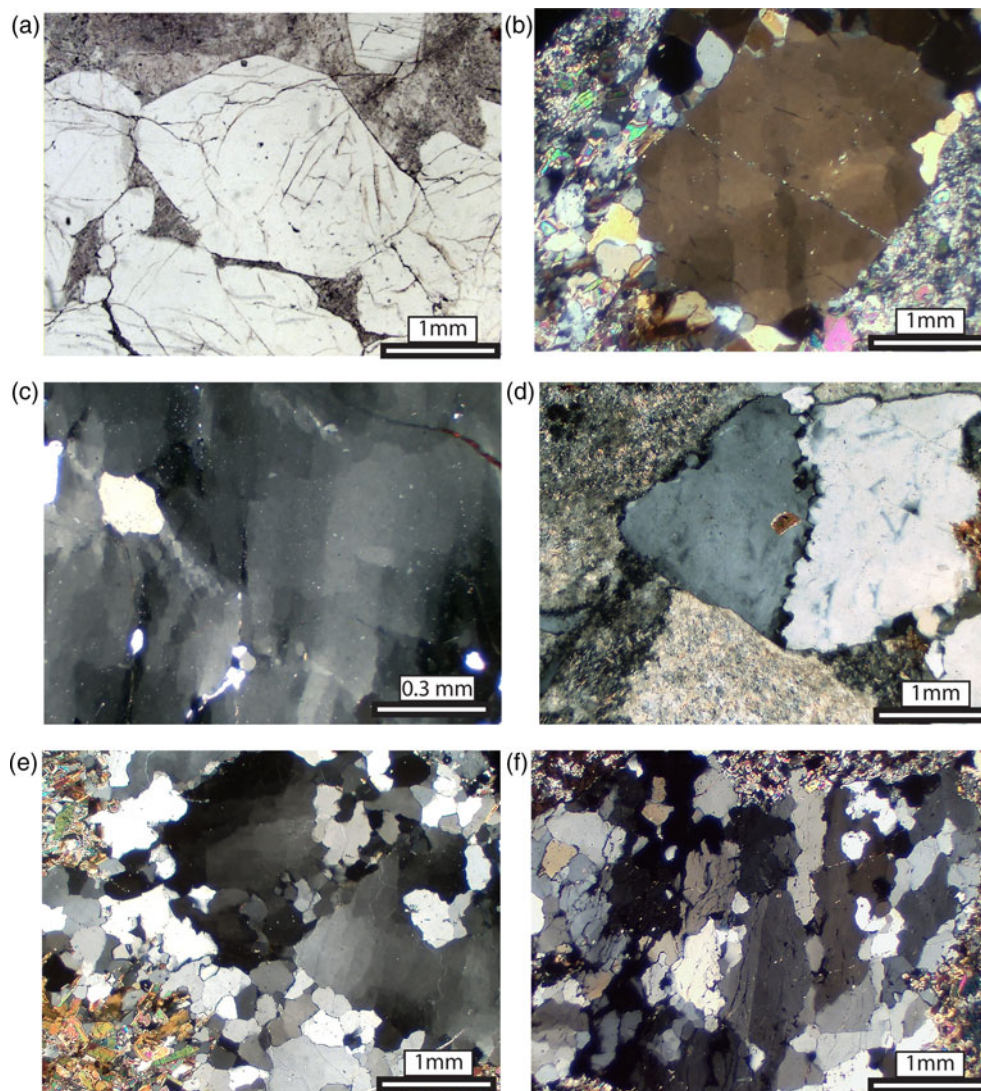


Fig. 3. (a–c) Photomicrographs showing variations of quartz microstructures in the quartz-rich domain 1. (a) Sample TMG01: PPL image showing euhedral quartz grains with face contacts. (b) Sample TMG05: crossed-polars image showing chessboard subgrains strongly developed parallel to the quartz c-axis, with recrystallisation along grain boundaries. (c) Sample TMG04: crossed-polars image showing chessboard subgrains within a relict quartz grain with some fine-grained recrystallisation internal to the grain. (d) Sample TMG08: crossed-polars image showing euhedral quartz grains with irregular lobate grain boundaries. (e) Sample TMG04: crossed-polars image showing relict quartz grains with elongate subgrains and recrystallisation along grain boundaries. (f) Sample TMG06: crossed-polars image showing quartz domains with a palisade texture and grain boundary migration along column boundaries.

0.61. The replacement of garnet is most commonly observed in granite enclaves (e.g. TMG03) in which garnet + mica domains are intergrown with radial quartz rosettes. Kyanite appears to be less abundant in the fine micaceous matrix than it is in garnet, and it is absent from the coarse micas.

The composition of the garnet + mica domain from EDS is given in Table 3. Notably, the domain-scale composition represents that of cordierite (basic formula $(\text{Fe,Mg})_2\text{Al}_4\text{Si}_5\text{O}_{18}$) with additional K and H_2O . Accordingly, we interpret the garnet + mica domains as hydrated and chemically altered pseudomorphs after cordierite.

U–Pb Monazite Geochronology

Monazite is commonly associated with the garnet + mica domains, though is also found as inclusions in igneous micas, particularly biotite (Fig. 8a–d). Monazite occurs as rounded

grains, $\sim 50 \mu\text{m}$ in diameter. Back-scattered electron imaging reveals no zoning. The weighted mean $^{206}\text{Pb}/^{238}\text{U}$ age of the concordant analyses (40% of total analyses) is taken as the time of monazite formation and yields an age of $474.0 \pm 11.6 \text{ Ma}$, $\text{MSWD} = 1.5$ (Fig. 8e). The high mean square weighted deviation (MSWD) indicates that even this age estimate, derived from concordant analyses, involves a variable amount of discordance, probably due to both incorporation of small amounts of common lead, and to minor disturbance of the isotopic system during younger events. The latter is compatible with the fact the Tso Moriri Complex underwent high pressure metamorphism during the Eocene (e.g. de Sigoyer *et al.* 1997, St-Onge *et al.*, 2013).

Pressure-temperature constraints

The phase equilibrium model (Fig. 9) was constructed using the bulk composition of a representative area in a garnet + mica

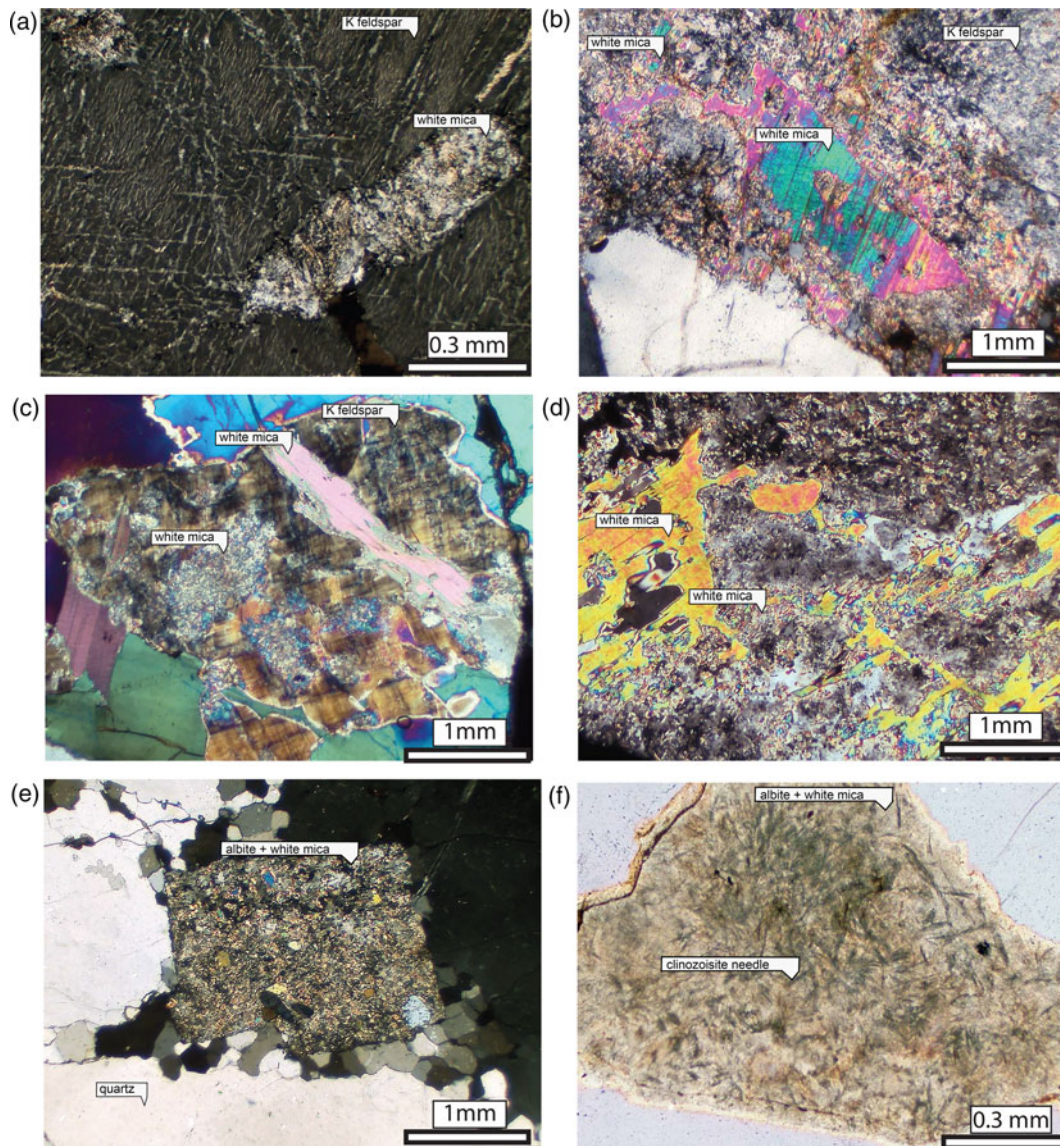


Fig. 4. Photomicrographs of feldspars in K feldspar + white mica (2) and albite + white mica (3) domains. (a) K-feldspar + white mica domain (sample TMG02): crossed-polars image showing perthitic texture in K-feldspar with an approximately rectangular inclusion replaced by white mica. (b) K-feldspar + white mica domain (Sample TMG02): crossed-polars image showing cloudy K-feldspar crystal with coarse white micas surrounded by finer phengitic white mica. (c) K-feldspar + white mica domain (sample TMG11): crossed-polars image showing a relict microcline crystal with a large cross-cutting white mica and patchy domains of fine-grained white mica. (d) K-feldspar + white mica domain (sample TMG08): crossed-polars image showing coarse-grained skeletal white mica with an irregular outline in a domain of fine-grained white mica + albite. (e) Albite + white mica domain (sample TMG04): crossed-polars image showing rectangular domain of white mica + albite surrounded by quartz with recrystallisation by grain boundary migration along grain boundaries. (f) Albite + white mica domain (sample TMG11): crossed-polars image showing albite + white mica with needles of clinozoisite in radial structures.

domain, approximating a homogeneous and chemically isolated domain with abundant hydrous phases, which might be expected to record prograde metamorphism. Several features support restricted chemical exchange between this domain and others: the preservation of cordierite stoichiometry in the less mobile elements Si, Al, Fe and Mg, the very low concentration of Ca and Mn in the garnets, and the Mg-rich nature of biotite. In contrast, the microstructures in other domains, such as the narrow coronas on igneous micas, display textural and compositional disequilibrium, and are not suitable for P–T determination.

The bulk composition (Table 3) falls almost entirely in the simpler KFMASH system, with very minor amounts of MnO, Na₂O, CaO and TiO₂. The uncertainties on these small amounts

are relatively large, however they have almost no effect on the overall phase relationships that are critical for determining pressure–temperature conditions. MnO is mainly accommodated in garnet, and TiO₂ in biotite. Outside the stability field of biotite, the model predicts minor ilmenite at lower P, rutile at higher P. CaO is a very minor component in garnet, and plagioclase is predicted only at low P in the sillimanite field. Na₂O is accommodated in muscovite, except at the highest pressures, where a tiny amount of Na-rich pyroxene or Na-mica is predicted (Fig. 9). Isoleths were determined for critical mineral properties, i.e. the modal abundance and pyrope content of garnet, the Si content of phengitic muscovite, and the stability limit and modal abundance of kyanite, using mineral composition ranges

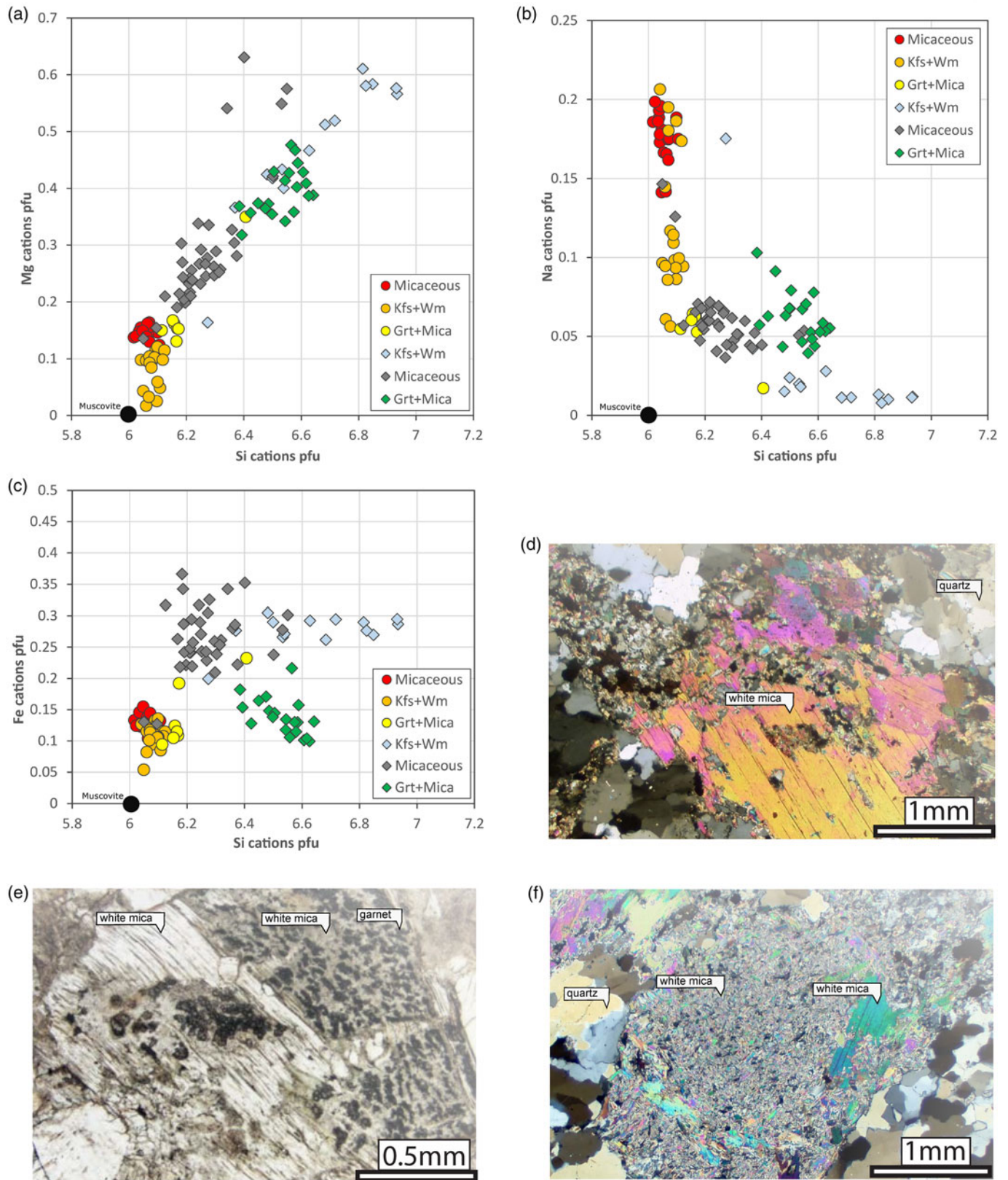


Fig. 5. Compositional data and photomicrographs of white micas. (a–c) White mica compositions for different domains. Circles = coarse-grained white mica, diamonds = fine-grained white mica. Pure muscovite end-member (black circle) Si = 6 pfu, total Al = 6. Phengite end-member Si = 7 pfu, Mg + Fe = 1 pfu, total Al = 4 pfu. Paragonite end-member Si = 6 pfu, total Al = 6 pfu, Na = 2 pfu. (d) Sample TMG08: crossed-polars image showing coarse white mica with fine white mica at the rim in K-feldspar + white mica domain 2. (e) Sample TMG01: PPL image showing coarse-grained white mica of skeletal habit, associated with fine white mica and garnet, in garnet + mica domain 5. (f) Sample TMG08: crossed-polars image showing fine white mica aggregate with remnants of coarse white mica in K-feldspar + white mica domain 2.

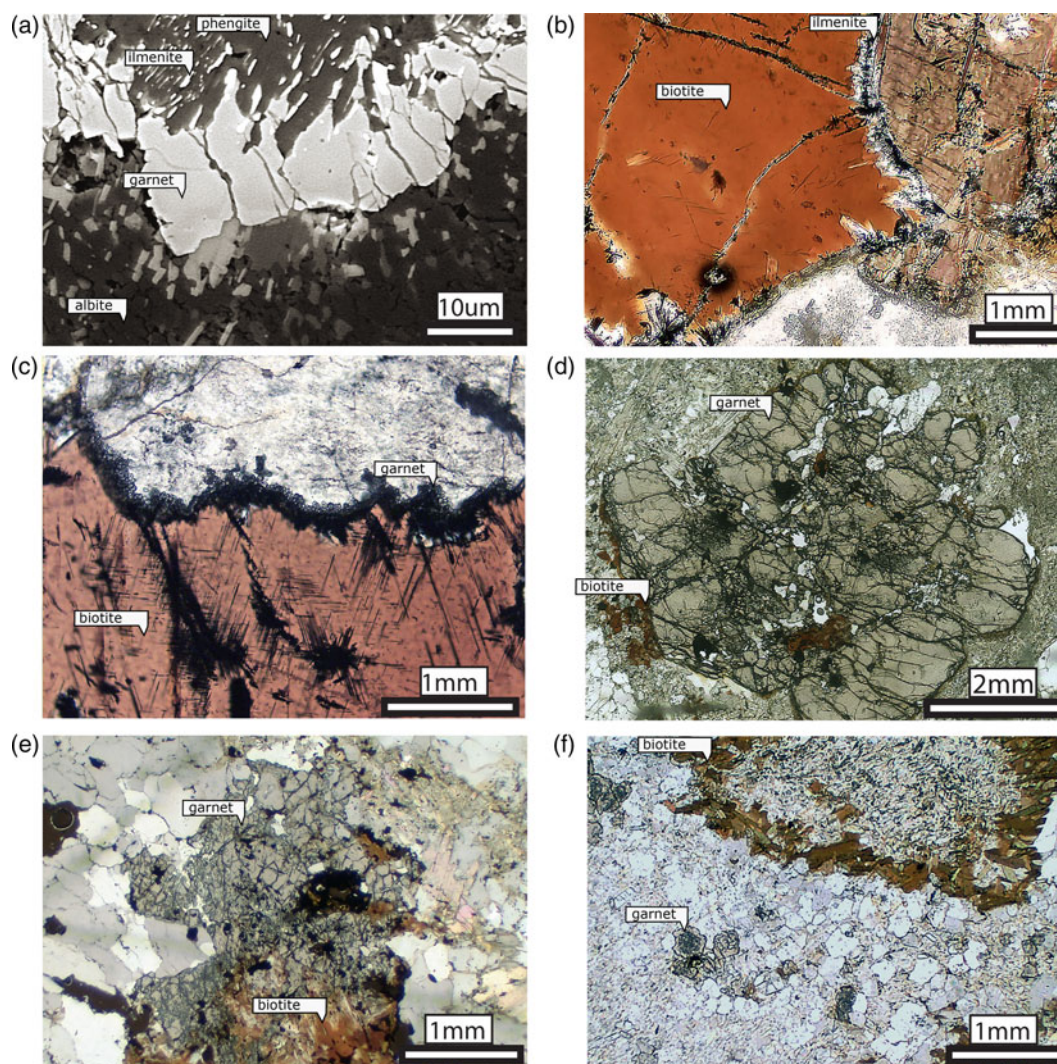


Fig. 6. Photomicrographs of biotite in the micaceous domain 4. (a) Sample TMG01: BSE image of zoned garnet rim and intergrown ilmenite and phengite around igneous biotite (top = micaceous domain 4) in contact with albite + white mica (bottom = albite + white mica domain 3). (b) Sample TMG01: PPL image showing red biotite cluster with phengite + ilmenite intergrowth replacing biotite along the grain boundary. (c) Sample TMG01: PPL image showing granular garnet texture around igneous biotite. (d) Sample TMG06: coarse garnet with a thin rim of brown biotite. (e) Sample TMG06: PPL image showing garnet replacing red biotite aggregate. (f) Sample TMG04: PPL image showing white mica with biotite aggregate around the rim, commonly associated with garnets. Zoned garnets replacing rectangular biotite inclusions within K feldspar + white mica domain 2 (bottom).

determined in the same domain that was used to determine the bulk composition.

Garnet is present throughout the P–T region of interest on Fig. 9, but has an interval of rapid prograde growth, shown as a pink band, accounting for at least half of the final garnet volume. Almost no further growth is predicted in the broad HP–HT fields above 600°C and 15 kbar. The observed pyrope mole fraction in garnet lies between 0.18 and 0.26. This variation corresponds to the predicted garnet growth spurt, up to the maximum volume proportion seen in the domain analysed. Essentially all kyanite growth is predicted to occur, at the expense of chloritoid, over a narrow (c. 6°C) temperature interval. This band cuts obliquely across the interval of rapid garnet growth, such that above ~26 kbar, kyanite has completed its growth at the beginning of the rapid increase in garnet, thereby allowing garnet to trap abundant kyanite inclusions. In contrast, at $P < \sim 22$ kbar, kyanite does not appear until garnet is almost fully grown. Thus, the entrapment of kyanite inclusions in garnet at high pressure is

consistent with the P–T path deduced from metabasic eclogites (grey arrows a and b). The interval of kyanite and garnet growth corresponds to a predicted silica content in phengite of ~6.6 per formula unit of 22 (O), matching the upper part of the range in fine-grained white mica in the domain. Therefore, we conclude that the garnet-bearing assemblage in this domain type formed during prograde eclogite-facies metamorphism at c. 550–650°C, >25 kbar.

Interpretation of magmatic-metamorphic evolution in domains

The five textural domains found in the Tso Morari granitoids can be interpreted as originating from the distribution of primary igneous minerals, i.e.: (1) magmatic quartz; (2) magmatic K-feldspar, with its inclusions; (3) magmatic plagioclase; (4) magmatic muscovite and biotite; and (5) cordierite. When taken together with the record of subsequent chemical and microstructural modification,

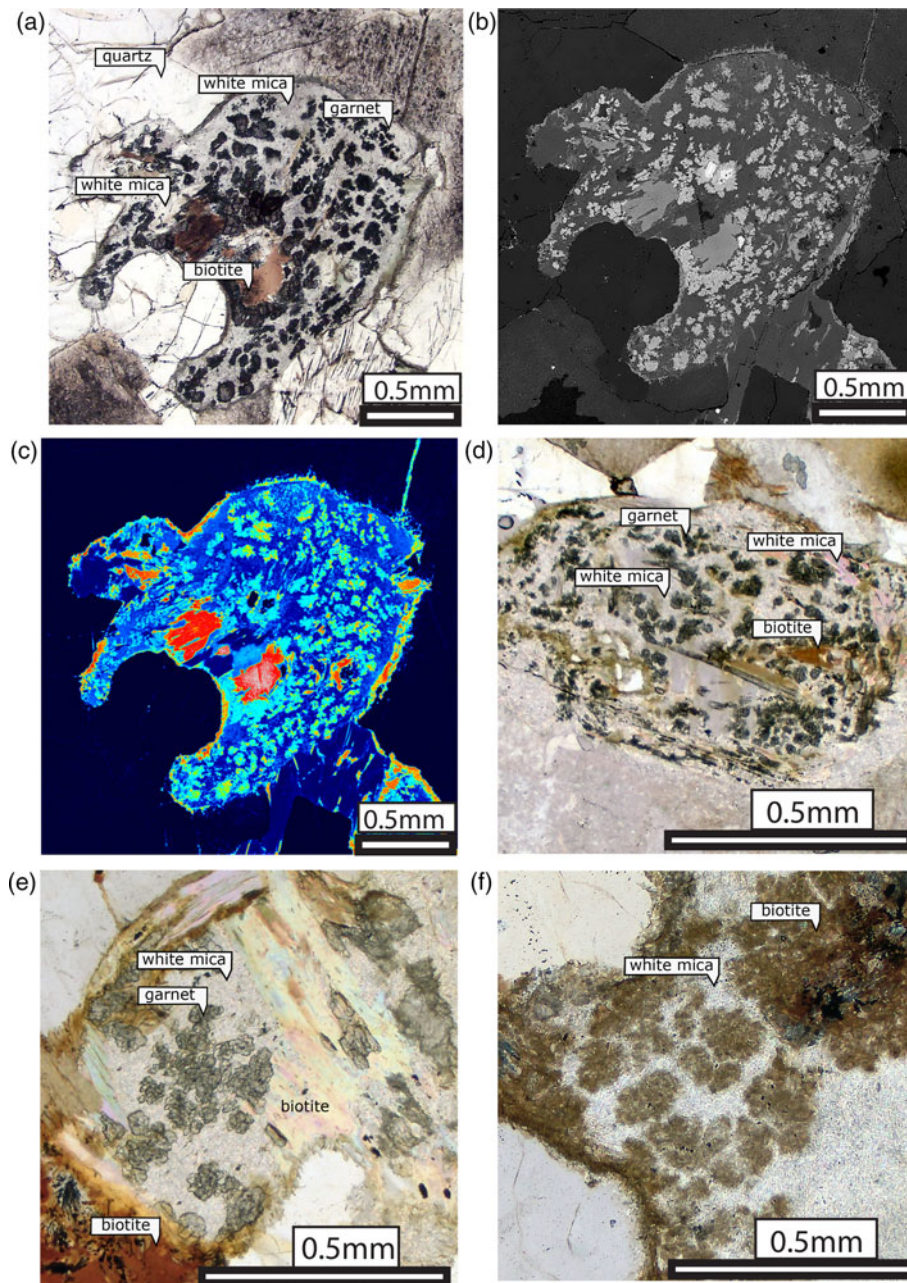


Fig. 7. Photomicrographs of garnet + mica domain. (a) Sample TMG01: cordierite pseudomorph with large brown biotite, dark garnets and a matrix of fine-grained white mica. (b) Sample TMG01: BSE image of cordierite pseudomorph showing bright garnets and fine-grained white mica matrix. (c) Sample TMG01: EDS Mg map of cordierite pseudomorph with Mg-rich biotite (red), garnet (pale blue) and white mica (dark blue). (d and e) Sample TMG09: coarse biotite and white mica of skeletal habit around the edge, associated with fine white mica and garnet. (f) Sample TMG02: garnets completely replaced by brown biotite.

the five microdomains collectively preserve a sequence of events that includes the following four stages (Fig. 10): (1) magmatic crystallisation; (2) late-magmatic hydrothermal alteration; (3) (ultra) high-pressure metamorphism; and (4) Barrovian metamorphism with attendant regional deformation. In this section we discuss the evidence that supports a protracted magmatic–metamorphic evolution of the Tso Morari granites. The inferred mineral assemblage associated with each event is recorded in Table 4.

Magmatic crystallisation

Primary (igneous) mineral microstructures of quartz, K-feldspar, biotite and muscovite are partially preserved in most samples. The idiomorphic and bipyramidal microstructures in quartz domains indicate that many of the primary igneous quartz grains have been generally unaffected by subsequent events. Euhedral quartz grains

cluster into aggregates with interstitial feldspar, suggesting that quartz was one of the first phases on the liquid line of descent. That the quartz–quartz grain boundaries form along well-developed crystal facets (Fig. 3a) indicates quartz underwent synneusis; the mutual attachment of crystals in a melt (Vance, 1969). These sintering microstructures imply that: (1) quartz grains were crystallised early during the magma solidification process when their growth would not have been impinged by other solid phases; and (2) quartz crystals were able to move freely (i.e. in suspension) prior to attachment in low energy grain-boundary configurations (Swanson and Fenn, 1986; Dyck and Holness, 2022).

K-feldspar megacrysts are also interpreted here as being magmatic in origin. The megacrysts contain inclusions of both single crystals and aggregates of phases which correspond to the different primary igneous domain types described in this paper.

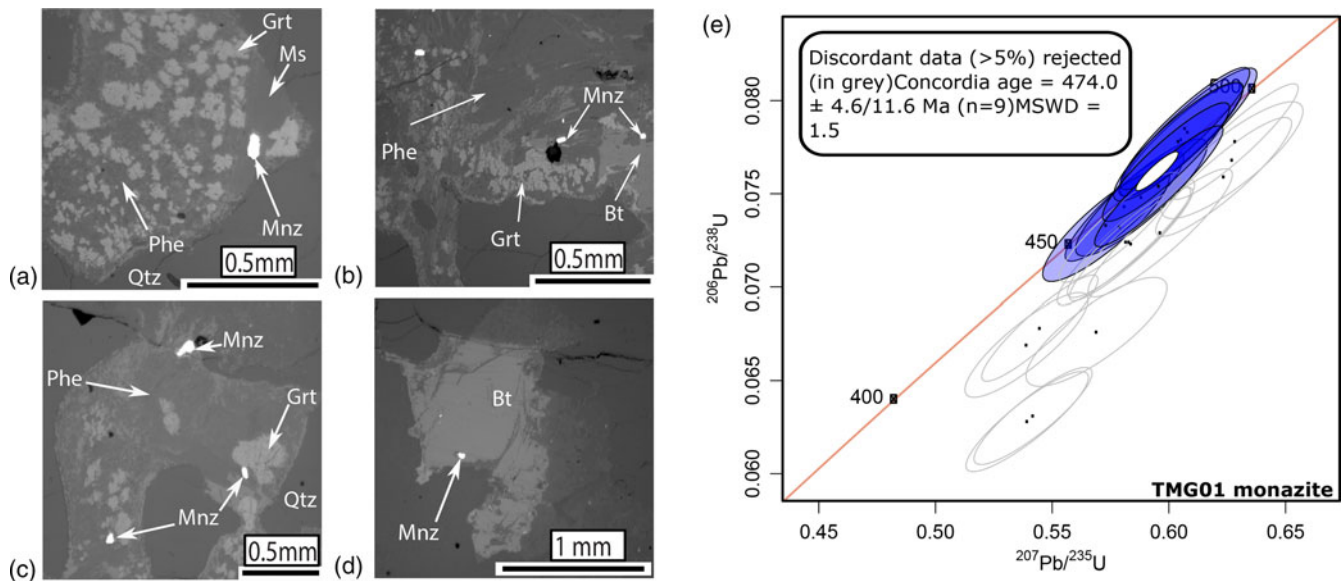


Fig. 8. (a–c) BSE images of monazite in pseudomorphs after cordierite (garnet + mica domain). (d) BSE image of monazite in igneous biotite (micaceous domain). (e) Wetherill concordia plot showing concordant (blue) and non-concordant (grey) analyses of monazite from sample TMG01; concordia centroid shown as white ellipse. Ellipses and ages are shown and quoted at 2σ .

These mineral inclusions are distinctly smaller than the phases and aggregates outside the megacrysts, and they may reflect the incipient stages of crystallisation of primary igneous minerals from the magma over which the megacrysts initially grew. The now preserved K-feldspar is perthitic, occasionally showing microcline twinning (Fig. 4c), indicating that the magma was hydrous (Parsons *et al.*, 1971).

Further evidence for an earlier magmatic history is found in the coarse-grained muscovite which occurs as clusters in the matrix and is associated with coarse-grained Ti-rich biotite and polycrystalline biotite aggregates. The relatively high Ti content of biotite is indicative of a high-temperature magmatic origin (Forbes and Flower, 1974; Robert, 1976; Tronnes *et al.*, 1985; Abrecht *et al.*, 1988). Though the polycrystalline aggregates might not necessarily be primary igneous in nature, their high Ti content is consistent with them forming by the recrystallisation of primary coarse-grained biotite while the granite was still at elevated temperatures.

Late-magmatic hydrothermal alteration

Plagioclase and cordierite are both interpreted as being part of the original igneous assemblage, however, their compositions no longer reflect the primary mineral composition expected in igneous rocks and thus we interpret them as having undergone late- to post-magmatic hydration/metasomatic alteration. Several features are analogous to textures of late-magmatic alteration that are commonly observed in unmetamorphosed peraluminous granites. An example is the partial replacement of K-feldspar with laths or skeletal networks of muscovite, as in the Land's End granite, Cornwall, UK (Booth, 1968) and the anatectic biotite-granite from the Trois Seigneurs Massif, Pyrenees (Fig. 11a–b) (Wickham, 1987). Equivalent microstructures from the Tso Morari metagranite are shown in Fig. 11c–d, indicating that these experienced a similar alteration prior to metamorphism. Moreover, the composition of these muscovites is comparable

with that of magmatic white micas in the same samples (Fig. 5a–c).

The bulk composition of the garnet + mica domain resembles a cordierite composition with additional K and H_2O . It is common in peraluminous granites for cordierite to destabilise upon cooling, causing it to break down during hydrothermal alteration to muscovite, phlogopite/biotite and/or chlorite (Booth, 1968; Farina *et al.*, 2012). Unmetamorphosed examples of this can be found in the Peninsula granite of the Cape Granite Suite, South Africa (Farina *et al.*, 2012, their figure 4a), and biotite granite from the Trois Seigneurs Massif (Fig. 12a–b) (Wickham, 1987). In the Land's End granite of the Cornubian batholith in Cornwall, England both pinitised cordierite and secondary muscovite are associated with late- to post-magmatic alteration (Booth, 1968; Exley *et al.*, 1982; Hawkes and Dangerfield, 1978). In the Peninsula granite, cordierite is a common phase in the enclaves within the granite, where it has been replaced by a mineral assemblage involving “aggregates of green-brown Ti-poor biotite and white mica as well as by very fine-grained mats of phyllosilicates varying under the polar microscope from grey to the typical third order blue of muscovite” (Farina *et al.*, 2012), which we interpret as being replaced partly by coarser-grained micas at higher temperature, and subsequently by pinite.

In the Tso Morari metagranites, coarse-grained muscovite and Ti-poor, Mg-rich biotite commonly form rims around the edge of the cordierite pseudomorphs, with fine-grained aggregates of phengite at the core (Fig. 7a–e, 12c–d). This texture is also commonly observed in coarse-grained enclaves, indicating that these were composed originally of cordierite and quartz. The similarity in composition between the coarse-grained white mica in the cordierite pseudomorphs, compared with the igneous white mica (Fig. 5a–c), suggests that these also were formed during the late-stage hydrothermal alteration of the granite. The biotite within the cordierite pseudomorph has a high-Mg, low-Ti composition, consistent with formation by replacement of a relatively magnesian cordierite. Subsequent metamorphism of the fine-grained

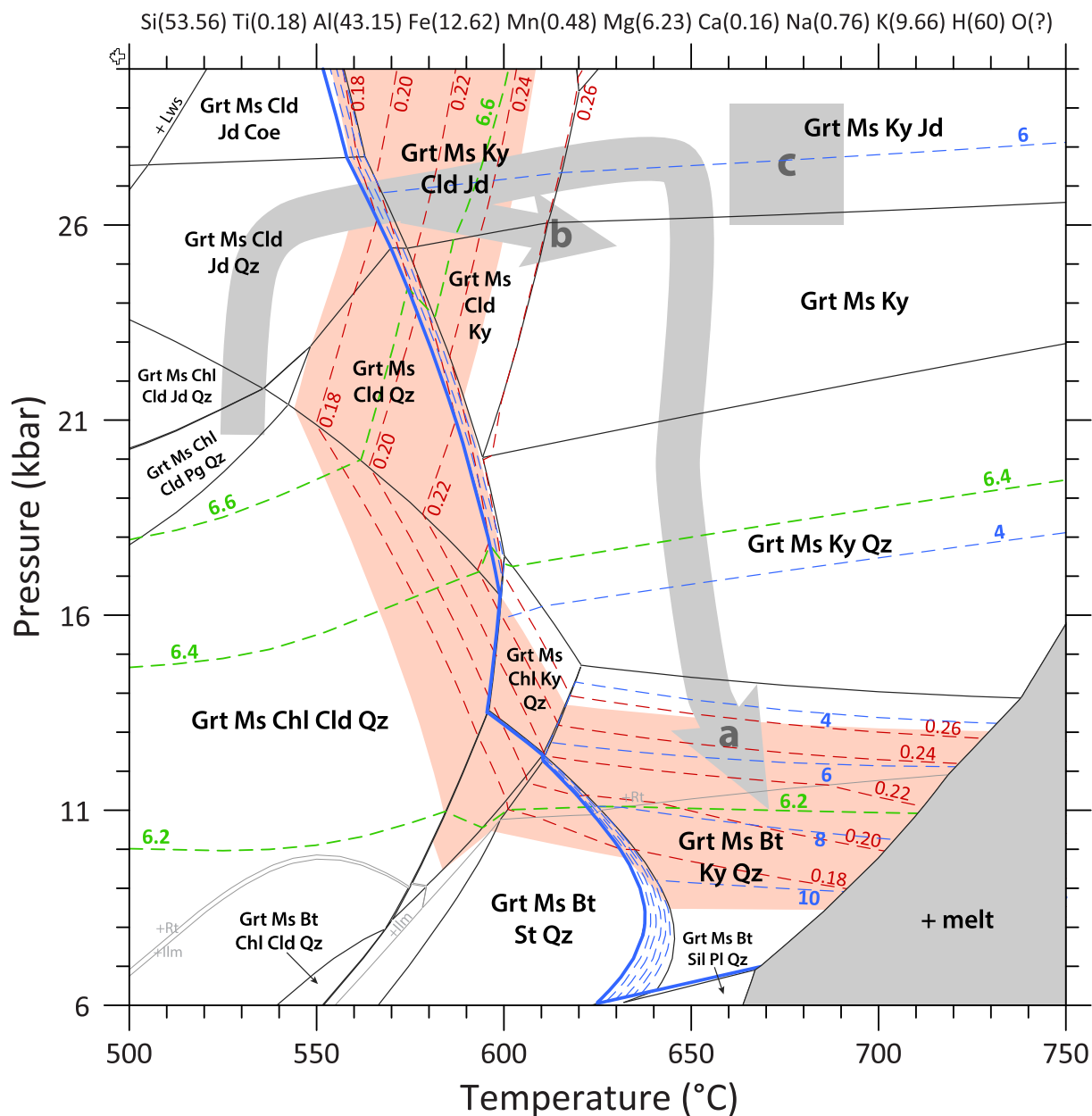


Fig. 9. Pressure-temperature equilibrium assemblage diagram for the composition of the garnet + mica (cordierite) domain, to account for the development of garnet with kyanite inclusions in a matrix of fine-grained phengitic white mica. Pale red band marks the interval of significant garnet growth; red dashed isopleths show the range of pyrope mole fraction (0.18 to 0.26) observed in garnet. Solid blue curve and blue dashed isopleths show first appearance and volume % of kyanite. Green dashed isopleths are Si content in white mica on the basis of 22(O); observed micas have 6.4 to 6.7 Si pfu. Grey paths and box show: (a) overall P-T path after St-Onge *et al.* (2013) and Palin *et al.* (2014), based on phase equilibrium modelling of zoned garnet in metabasic eclogite, overprinted eclogite, and amphibolite-facies re-equilibrated gneisses; (b) P-T path from outer zones of zoned garnet adjusted for fractionation of components, St Onge *et al.* (2013); and (c) peak conditions determined by Bidgood (2020), straddling the quartz-coesite transition.

micaceous pinite in the core of this domain resulted in the observed assemblage of garnet, kyanite and phengite.

Close association of monazite with pseudomorphs after cordierite may suggest that monazite formed either during crystallisation of the granite or else is associated with the breakdown of cordierite. However, cordierite does not typically contain rare earth elements (REE), so monazite is not likely to form by liberation of REE from cordierite, but is more probably associated with crystallisation of the granite. The U-Pb age of monazite of sample TMG01 is 474.0 ± 11.6 Ma (2s), and is within uncertainty of a single grain concordant U-Pb zircon age of 479 ± 2 Ma from the

Polokongka La granite, which is interpreted as the age of crystallisation from a granitic melt (Girard and Bussy, 1999).

(Ultra)high-pressure metamorphism

The presence of palisade quartz microstructures in sample TMG06 is particularly noteworthy as this microstructure has been demonstrated recently to have formed during the coesite-quartz transition (Bidgood *et al.*, 2021) and is a cryptic indicator of ultrahigh-pressure metamorphism in felsic rocks. The fact that palisade quartz is found in only a limited number of Tso Morari

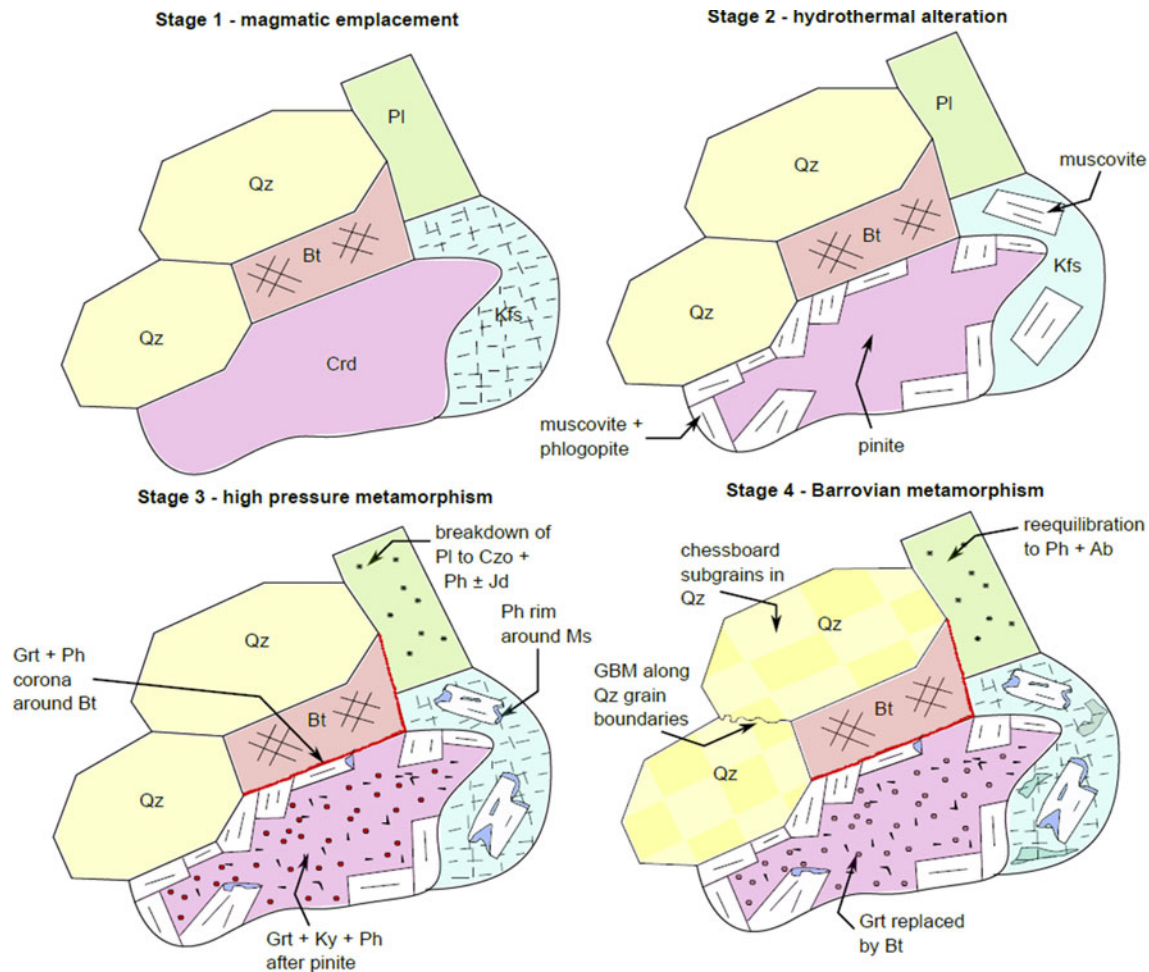


Fig. 10. Schematic representation of the four stages preserved within the Tso Morari metagranites within five microstructural domains.

granite samples, even though there are abundant quartz domains in all samples, probably demonstrates the rarity of forming and preserving this microstructure rather than a lower peak-pressure history for the Tso Morari granites.

Coronas of garnet + phengite around igneous biotite preserve evidence of biotite breakdown at high metamorphic pressures. In the Polokongka La granite this corona texture was interpreted by Girard and Bussy (1999) to form from the breakdown of igneous biotite at eclogite-facies conditions, and has been documented elsewhere in the Monte Mucrone metaquartz diorites of the Sesia Zone (Oberhänsli *et al.*, 1985; Koons *et al.*, 1987) and the Brossasco metagranite (Biino and Compagnoni, 1992) of

the European Alps, as well as the Yankou metagranite of the Sulu UHP province, China (Hirajima *et al.*, 1993). In the Tso Morari metagranites, garnet + phengite coronas around biotite are common, although volumetrically minor, indicating that all of these samples underwent a similar eclogite-facies metamorphic history.

The fine-grained parts of the garnet + mica domains, i.e. pseudomorphs after cordierite, contain the assemblage phengite + garnet + kyanite, expected to belong to the eclogite facies. This is confirmed by the results of phase equilibrium modelling discussed above in 'Pressure-temperature constraints', which indicate prograde metamorphism at >25 kbar pressure. Fine-grained white mica associated with coarse micas of igneous origin have compositions that plot along the celadonite exchange vector, suggesting recrystallisation at high pressure. The mineral assemblage and textures in this domain are comparable to the assemblage preserved in metamorphosed pseudomorphs after cordierite in the French Massif Central (Lotout *et al.*, 2017, their figure 3f).

The presence of clinozoisite needles in white mica + albite domains, i.e. former plagioclase, in TMG01 and TMG11, suggests a high-pressure metamorphic transformation. Although these domains now contain white mica rather than jadeite, the pattern and scale of the clinozoisite needles strongly resembles the distribution of (clino)zoisite within the jadeite-rich pseudomorphs after plagioclase in Monte Mucrone metaquartz-diorites (Koons *et al.*, 1987).

Table 4. Inferences of mineral paragenesis in the Tso Morari granites.

Magmatic stage	Late magmatic stage	High-pressure stage	Later modification
Quartz K-feldspar Plagioclase	muscovite	coesite phengite clinozoisite	quartz albite + white mica biotite
Ti biotite		phengite + ilmenite + garnet	biotite + albite biotite
Muscovite Cordierite	muscovite + Mg-rich biotite	phengite + garnet + kyanite	biotite + albite biotite

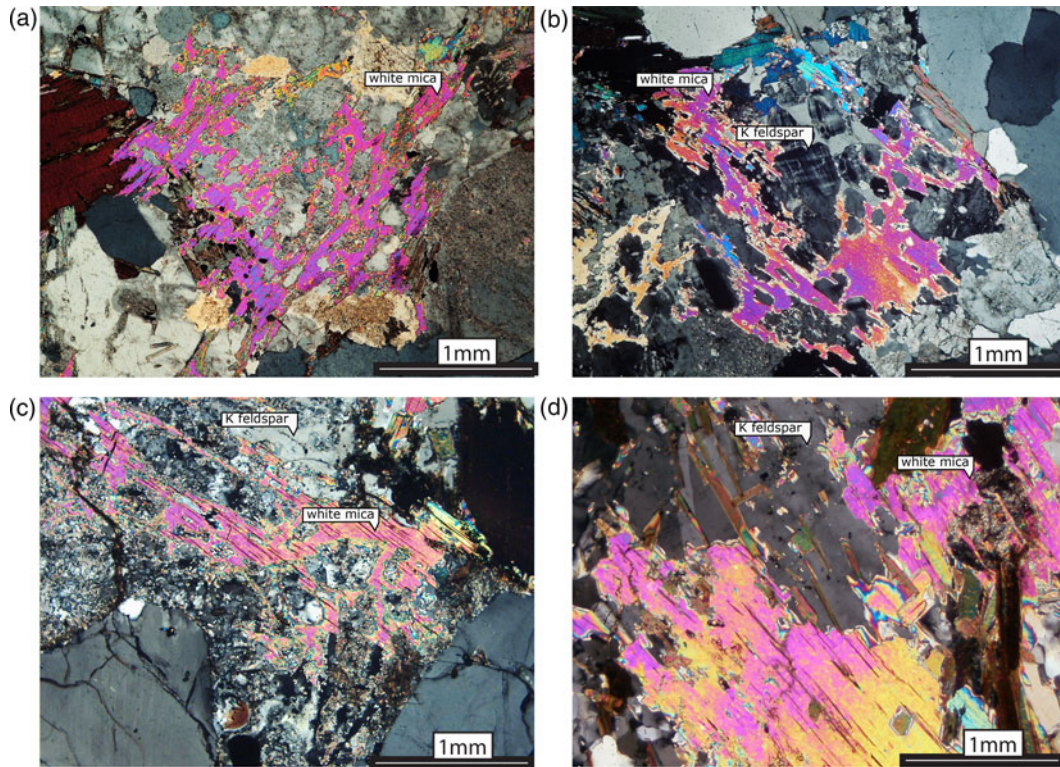


Fig. 11. (a, b) Skeletal muscovite forming after K-feldspar in the biotite granite described by Wickham (1987) in the Trois Seigneurs Massif. (c) Sample TMG02 from the Tso Morari Complex showing skeletal muscovite after K-feldspar. (d) Sample TMG05 showing coarse-grained irregular muscovite after K-feldspar (after Booth, 1968).

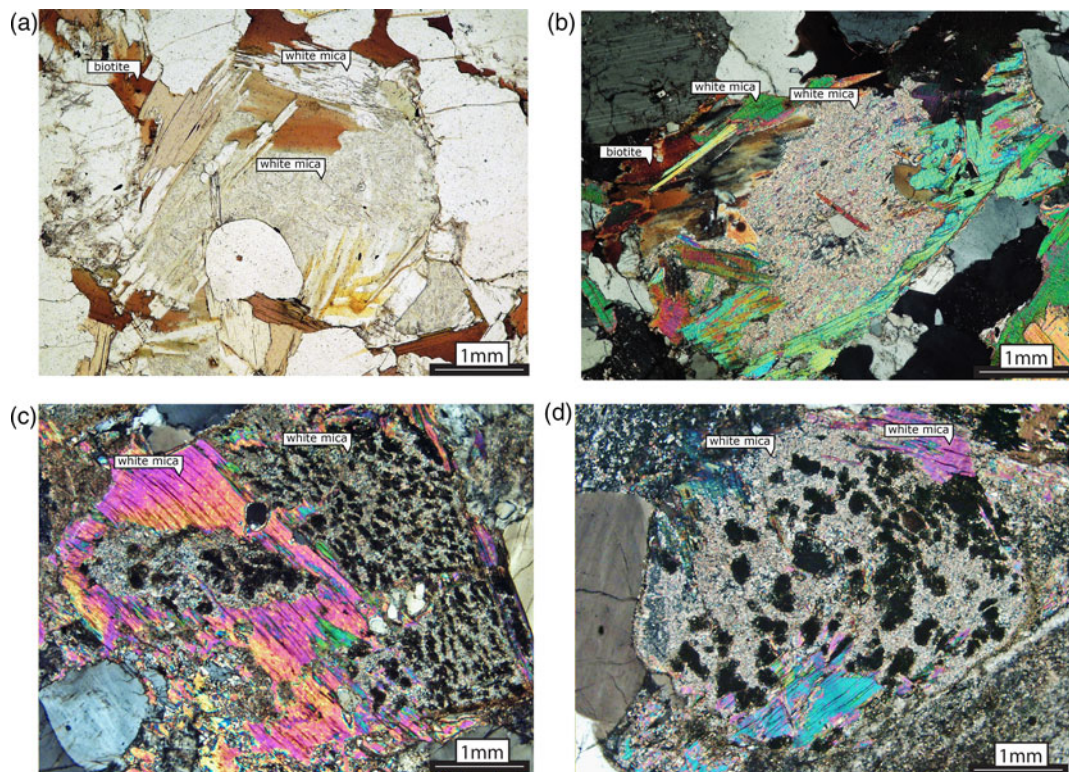


Fig. 12. Photomicrographs of cordierite pseudomorphs. (a) PPL image showing pinitised cordierite pseudomorph from biotite granite from the Trois Seigneurs Massif, with coarse-grained biotite and muscovite cross-cutting the domain. (b) Crossed-polars image showing pinitised cordierite pseudomorph from the Trois Seigneurs Massif, with coarse-grained biotite and white mica around the edge of the pseudomorph. (c) Sample TMG01 from the Tso Morari Complex: crossed-polars image showing a coarse white mica grain penetrating across a cordierite pseudomorph. (d) Sample TMG01 from the Tso Morari Complex: crossed-polars image showing coarse white mica around the edge of a cordierite pseudomorph.

In the Puga Gneiss, large idioblastic garnets are occasionally present in which a prograde to high-pressure metamorphic zoning pattern is preserved (Bidgood, 2020). The progression from thin coronitic rims of garnet (sample TMG01), to granular or skeletal replacement of red-brown biotite (sample TMG04) to euhedral garnets (sample TMG06) in increasingly metamorphosed samples, could represent a more complete transformation of biotite at eclogite-facies conditions, facilitated by the availability of fluid at high pressure.

Barrovian metamorphism with attendant deformation

Pressure and temperature paths from mafic eclogites in the Tso Morari Complex predict steep, approximately isothermal decompression from the eclogite-facies peak to amphibolite-facies conditions (Chatterjee and Jagoutz, 2015; de Sigoyer *et al.*, 1997; Guillot *et al.*, 1997; St-Onge *et al.*, 2013; Wilke *et al.*, 2015). The Tso Morari metagranites, in contrast to the Puga Gneiss, show limited evidence for mineral growth and re-equilibration under amphibolite-facies conditions. The extent of recrystallisation (e.g. of micas) appears to correlate with increasing strain.

Some insight can be obtained from the phase equilibrium modelling of the former cordierite domains (Fig. 9). During decompression to c. 15 kbar, very little change is predicted in mineral proportions or composition, however some re-equilibration may have occurred in the sample to account for Si contents in phengite decreasing to c. 6.4 pfu, and the corresponding increase in Al is perhaps coupled with an observed (and predicted) decrease in the amount of kyanite in the mica matrix, compared with that trapped in garnet. Under amphibolite-facies conditions (<15 kbar), biotite becomes stable, however almost no devolatilisation is predicted on decompression at c. 650°C. The implied reaction is essentially $\text{Grt} + \text{Ms} = \text{Bt} + \text{Ky} + \text{Qz}$, which (at constant K_2O) conserves H_2O , however there is no evidence that this reaction occurred. Instead, the observed replacement of garnet by biotite seen in many samples is not accompanied by new growth of an aluminium silicate (Ky or Sil). This simple replacement would require addition of external fluid, and a further implication would be that K_2O was also introduced in this fluid. In the absence of deformation, relatively little fluid is involved, as replacements are not always complete and the microstructures are not significantly modified.

The breakdown of garnet and its replacement by biotite could also suggest that the Puga Gneiss, strongly deformed under amphibolite-facies conditions and potentially fluid-saturated, given the extent of amphibolite-facies retrogression shown by the basic bodies it contains, has lost much of any garnet it developed at higher pressures.

The observation that plagioclase (white mica + albite) domains contain only hints that they were transformed to jadeite-bearing aggregates suggests either that much plagioclase was not converted to jadeite, or that jadeite and quartz were transformed to albite (and white mica) on decompression. It is also possible that plagioclase was extensively sericitised at low temperature during post-magmatic alteration. The latest features developed in the Tso Morari metagranites may relate to the low-strain deformation recorded in many samples. Deformation temperatures can be estimated by comparing observed quartz microstructures to qualitative temperature ranges for quartz deformation regimes (e.g. bulging, subgrain rotation and grain-boundary migration; Stipp *et al.*, 2002). High-temperature quartz microstructures in the form of chessboard subgrains are observed in granitoid samples from the Polokongka La (Fig. 3b,c,e) region of the Tso Morari

Complex. These microstructures are indicative of low-strain deformation at temperatures >550–600°C (Kruhl, 1996; Wallis *et al.*, 2019). Amoeboid shapes along grain boundaries are evidence for low-strain features of active, though limited, deformation in the grain-boundary migration regime at ~550°C (Stipp *et al.*, 2002). Metagranite samples from the Polokongka La region also display tabular subgrains internal to the grain, suggesting recovery associated with dislocation glide and climb at somewhat lower temperatures (Passchier and Trouw, 2005). Peak deformation temperatures of >600°C are consistent with electron back-scattered diffraction analysis of quartz in the Puga Gneiss across the Tso Morari Complex by Dutta and Mukherjee (2021).

Discussion

The incomplete transformation of metagranitoids at (ultra)high pressures

The scarcity of mineralogical evidence preserved in felsic rocks that have experienced (ultra)high pressures implies that either: (1) (ultra)high-pressure assemblages are not readily produced (i.e. low-pressure minerals persist in a metastable manner); or (2) (ultra)high-pressure assemblages form but are readily transformed to lower pressure assemblages upon decompression. The evidence we present here for the preservation of both igneous and late-magmatic hydrothermal alteration indicates the importance of hypothesis 1 in the absence of penetrative deformation, regardless of uncertainty over the extent of high-P breakdown of plagioclase to jadeite.

The Tso Morari metagranites underwent partial transformation in the eclogite facies. Examples of igneous textural domains, preserved despite later replacement of the igneous minerals, are found in low-strain igneous rocks such as the previously mentioned Monte Mucrone metaquartz diorite (Dal Piaz *et al.*, 1972; Oberhänsli *et al.*, 1985; Koons *et al.*, 1987; Zucali *et al.*, 2021), the Brossasco metagranites (Schertl *et al.*, 1991; Biino and Compagnoni, 1992) and the Yankou metagranite (Wallis *et al.*, 2007), as well as in the Kokchetav Massif in Kazakhstan (Zhang *et al.*, 1997). Additionally, in the Flaktraket mangerite-granulite complex in the Western Gneiss region of Norway, >95% of the complex is thought to have preserved metastable igneous textures and coronas around the magmatic orthopyroxene during eclogite-facies conditions (Wain *et al.*, 2001).

There are some marked differences between the Tso Morari metagranites and high-pressure metagranites from other terranes. For example, omphacite is expected to be the equilibrium pyroxene for felsic bulk compositions, and in the case of local equilibrium, plagioclase domains may be transformed to jadeite-rich aggregates (e.g. Koons *et al.*, 1987). However, sodic pyroxene was not observed in the feldspar domains of the Tso Morari granites. Nevertheless, textures preserved in the plagioclase domains, including the presence of arrays of clinzoisite needles similar to those in transformed plagioclase, and the lack of primary twin lamellae, suggest that most of the primary plagioclase did not survive high-pressure metamorphism. Therefore, on balance, we consider that clinopyroxene was present at high pressures in at least some of these rocks, however it was subsequently overprinted during exhumation.

Static transformation in granite can be limited to within igneous mineral-scale domains, where a local effective bulk composition is dominant and there is very little communication between domains. For example, Koons *et al.* (1987) observed

jadeite cores and omphacite rims within pyroxene, zoisite and quartz-bearing domains replacing igneous plagioclase in the Monte Mucrone metaquartz diorites. Initially, the formation of jadeitic clinopyroxene after plagioclase was controlled by the effective bulk composition of the igneous Na-rich plagioclase. Subsequent mineral changes during growth of clinopyroxene were interpreted to be a result of partial equilibration of local mineral domains to the bulk composition as the equilibration volume enlarged and recrystallisation was promoted by progressive deformation, rather than directly due to changes in pressure and temperature (Koons *et al.*, 1987).

Garnet + phengite + ilmenite coronas around biotite are a common feature of partially transformed granites in high-pressure terranes. Koons *et al.* (1987) provided a detailed interpretation of this texture in the Monte Mucrone metaquartz diorites, where the asymmetrical compositional zoning of grossular in garnet coronas surrounding biotite is attributed to the influence of the breakdown of plagioclase into jadeite + quartz, which acts as a source for CaO and Al₂O₃. The rate-determining step in this reaction is thought to be the diffusion of Al₂O₃ and CaO from the plagioclase domain to the biotite rim and also accounts for the asymmetric zoning pattern seen in the garnet coronas. Koons *et al.* (1987) suggest that the non-completion of the biotite breakdown reaction could be due to the decrease in diffusive flux owing to the growth of garnet and muscovite coronas, lengthening diffusive pathways and therefore reducing the chemical potential gradients. Alternatively, the production of Al₂O₃ and CaO may have ceased as the plagioclase breakdown reaction ran to completion. The presence of asymmetric compositional zoning in garnet may therefore be an indication of plagioclase breakdown in the eclogite facies.

Partial transformation within the Tso Morari metagranites was limited by the availability of H₂O at high pressure, leading to corona textures where reactions did not run to completion. There was little communication between igneous domains, indicated by the essentially isochemical transformation of hydrous domains such as metamorphosed cordierite pseudomorphs. The absence of 'typical' eclogite-facies mineral assemblages such as jadeite + quartz within plagioclase domains could be attributed to lack of preservation owing to the re-equilibration during Barrovian metamorphism, or to extensive pre-metamorphic sericitisation.

Conclusions

Low-strain metagranite domains are found within the Tso Morari Complex, and are observed in this investigation to preserve textural and compositional evidence of early and late magmatic-hydrothermal features, followed by later eclogite-facies metamorphism. The Tso Morari metagranites therefore provide a unique window into these early histories. The microstructure of the igneous domains, the assemblages and the mineral compositions in the Tso Morari metagranites reveal a complex evolution in which a peraluminous S-type granite was emplaced during the Ordovician at 474.0 ± 11.6 Ma and hydrothermally altered during the late stages of emplacement.

Eclogite-facies metamorphism led to the partial transformation of igneous biotite to form garnet + phengite coronas and the complete transformation of hydrous pseudomorphs after cordierite to garnet, phengite and kyanite during high-pressure metamorphism, indicating prograde metamorphism at >25 kbar. The relatively low abundance of diagnostic high-pressure textures in the Tso Morari

metagranites and preservation of igneous minerals such as mica indicates that metamorphic transformations were limited by fluid availability, and controlled by mineral-scale compositional domains in the rock. In cases where transformation occurred in the eclogite facies, the absence of characteristic minerals such as jadeite may be attributed to overprinting during Barrovian metamorphism where H₂O was more readily available, leading to partial re-equilibration of original feldspar and cordierite domains.

The metagranites stand in marked contrast to their host rock, the high-strain Puga Gneiss, which contains amphibolite-facies mineral assemblages, fabric development and recrystallisation having erased almost all of its earlier history. The Tso Morari metagranites draw attention to the role of low strain and lack of fluid availability in preserving the original features and revealing the P–T history of continental basement rocks.

Acknowledgements. This work was funded by the Natural Environmental Research Council, grant number NE/L002612/1 awarded to AKB. Fieldwork to Ladakh was undertaken in 2016 and 2017 as part of the PhD of AKB and was partially funded by the Geological Society of London Mike Coward fund, the Mineralogical Society of Great Britain and Ireland, Edinburgh Geological Society, University College Oxford and the Royal Geographical Society.

The illustrated biotite granite sample from the Trois Seigneurs massif, eastern Pyrenees, was collected in 1984 by DJW on a field excursion led by R.S.J. Sparks and S.M. Wickham, supported by the Department of Earth Sciences, University of Cambridge. The sample L08-04 (TMG11) was collected in 2008 by M.P. Searle. Thanks to Jon Wade and Phil Gopon from Oxford University for help and training on the SEM and EMPA.

We would like to thank Michael Anenburg and two anonymous reviewers for their constructive comments on this manuscript.

Supplementary material. To view supplementary material for this article, please visit <https://doi.org/10.1180/mgm.2022.121>

References

- Abrecht J. and Hewitt D.A. (1988) Experimental evidence on the substitution of Ti in biotite. *American Mineralogist*, **73**, 1275–1284.
- Aleinikoff J.N., Schenck W.S., Plank M.O., Srogi L.A., Fanning C.M., Kamo S.L. and Bosbyshell H. (2006) Deciphering igneous and metamorphic events in high-grade rocks of the Wilmington complex, Delaware: Morphology, cathodoluminescence and backscattered electron zoning, and SHRIMP U–Pb geochronology of zircon and monazite. *Bulletin of the Geological Society of America*, **118**, 39–64.
- Austrheim H. (1986) Eclogitization of lower crustal granulites by fluid migration through shear zones. *Earth and Planetary Science Letters*, **81**, 221–232.
- Austrheim H. and Engvik A.K. (1997) Fluid transport, deformation and metamorphism at depth in a collision zone. Pp. 123–137 in: *Fluid Flow and Transport in Rocks*. Springer Netherlands.
- Austrheim H. and Griffin W. (1985) Shear deformation and eclogite formation within granulite-facies anorthosites of the Bergen Arcs, Western Norway. *Chemical Geology*, **50**, 267–281.
- Bidgood A.K. (2020) *The Petrology and Transformation History of Continental Crust in the Tso Morari Complex, Ladakh, Himalaya*. PhD thesis, University of Oxford. Available at: <https://ora.ox.ac.uk/objects/uuid:966a9121-82fc-4567-afbf-2bbcd55de04e>.
- Bidgood A.K., Parsons A.J., Lloyd G.E., Waters D.J. and Goddard R.M. (2021) EBSD-based criteria for coesite-quartz transformation. *Journal of Metamorphic Geology*, **39**, 165–180.
- Biino G.G. and Compagnoni R. (1992) Very-high pressure metamorphism of the Brossasco coronite metagranite, southern Dora Maira Massif, Western Alps. *Schweizerische Mineralogische und Petrographische Mitteilungen*, **72**, 347–363.
- Booth B. (1968) Petrogenetic significance of alkali feldspar megacrysts and their inclusions in Cornubian granites. *Nature*, **217**, 1036.

- Buick I.S., Lana C. and Gregory C. (2011) A LA-ICP-MS and SHRIMP U/Pb age constraint on the timing of REE mineralisation associated with Bushveld granites, South Africa. *South African Journal of Geology*, **114**, 1–14.
- Chatterjee N. and Jagoutz O. (2015) Exhumation of the UHP Tso Morari eclogite as a diapir rising through the mantle wedge. *Contributions to Mineralogy and Petrology*, **169**, 3.
- Chopin C. (1984) Coesite and pure pyrope in high-grade blueschists of the Western Alps: a first record and some consequences. *Contributions to Mineralogy and Petrology*, **86**, 107–118.
- Coggon R. and Holland T. (2002) Mixing properties of phengitic micas and revised garnet-phengite thermobarometers. *Journal of Metamorphic Geology*, **20**, 683–696.
- Cuthbert S.J. and Carswell D.A. (1982) Petrology and tectonic setting of eclogites and related rocks from the Dalsfjord area, Sunnfjord, west Norway. *Terra Cognita*, **2**, 315–316.
- Cuthbert S.J., Carswell D.A., Krogh-Ravna E.J. and Wain A. (2000) Eclogites and eclogites in the Western Gneiss region, Norwegian Caledonides. *Lithos*, **52**, 165–195.
- Dal Piaz G.V. Hunziker J.C. and Martinotti G. (1972) La Zona Sesia – Lanzo e l'evoluzione tettonico-metamorfica delle Alpi Nordoccidentali interne. *Memorie della Società Geologica Italiana*, **11**, 433–460 [available at: <https://ci.nii.ac.jp/naid/10026535850/>].
- de Sigoyer J., Guillot S., Lardeaux J.-M. and Mascle G. (1997) Glaucophane-bearing eclogites in the Tso Morari dome (eastern Ladakh, NW Himalaya). *European Journal of Mineralogy*, **128**, 197–212.
- Dutta D. and Mukherjee S. (2021) Extrusion kinematics of UHP terrane in a collisional orogen: EBSD and microstructure-based approach from the Tso Morari Crystallines (Ladakh Himalaya). *Tectonophysics*, **800**, 228641.
- Dyck B. and Holness M. (2022) Microstructural evidence for convection in high-silica granite. *Geology*, **50**, 295–299, <https://doi.org/10.1130/G49431.1>
- Epard J. and Steck A. (2008) Structural development of the Tso Morari ultra-high pressure nappe of the Ladakh Himalaya. *Tectonophysics*, **451**, 242–264.
- Exley C.S., Stone M. and Lees G.L. (1982) Petrology of the granites and minor intrusions. Pp. 293–302 in: *Igneous Rocks of the British Isles*. Wiley, Chichester, UK.
- Farina F., Stevens G. and Villaros A. (2012) Multi-batch, incremental assembly of a dynamic magma chamber: the case of the Peninsula pluton granite (Cape Granite Suite, South Africa). *Mineralogy and Petrology*, **106**, 193–216.
- Forbes W.C. and Flower M.F.J. (1974) Phase relations of titan-phlogopite, $K_2Mg_4TiAl_2Si_4O_{20}(OH)_4$: A refractory phase in the upper mantle? *Earth Planetary Science Letters*, **22**, 60–66.
- Fuchs G. and Linner M. (1996) On the geology of the suture zone and Tso Morari dome in Eastern Ladakh (Himalaya). *Jahrbuch der Geologischen Bundesanstalt*, **139**(191), 207.
- Gebauer D., Schertl H.P., Brix M. and Schreyer W. (1997) 35 Ma old ultrahigh-pressure metamorphism and evidence for very rapid exhumation in the Dora Maira Massif, Western Alps. *Lithos*, **41**, 5–24.
- Girard M. and Bussy F. (1999) Late Pan-African magmatism in the Himalaya: new geochronological and geochemical data from the Ordovician Tso Morari metagranites (Ladakh, NW India). *Schweizerische Mineralogische und Petrographische Mitteilungen*, **79**, 399–418.
- Guillot S., Sigoyer J. De and Lardeaux J. (1997) Eclogitic metasediments from the Tso Morari area (Ladakh, Himalaya): Evidence for continental subduction during India-Asia convergence. *Contributions to Mineralogy and Petrology*, **128**, 197–212.
- Hawkes J. and Dangerfield J. (1978) The Variscan granites of south-west England: a progress report. *Proceedings of the Ussher Society*, **4**, 158–171.
- Hirajima T., Wallis S.R., Zhai M. and Ye K. (1993) Eclogitized metagranitoid from the Su-Lu ultra-high pressure (UHP) province, eastern China. *Proceedings of the Japan Academy, Series B*, **69**, 249–254.
- Holland T.J.B. and Powell R. (1998) An internally consistent thermodynamic data set for phases of petrological interest. *Journal of Metamorphic Geology*, **16**, 309–343.
- Holland T. and Powell R. (2003) Activity–composition relations for phases in petrological calculations: an asymmetric multicomponent formulation. *Contributions to Mineralogy and Petrology*, **145**, 492–501.
- Horstwood M.S., Košler J., Gehrels G., Jackson S.E., McLean N.M., Paton C., Pearson N.J., Sircombe K., Sylvester P., Vermeesch P. and Bowring J.F. (2016) Community-derived standards for LA-ICP-MS U-(Th)- Pb geochronology–Uncertainty propagation, age interpretation and data reporting. *Geostandards and Geoanalytical Research*, **40**, 311–332.
- Koons P.O., Rubie D.C. and Frueh-Green G. (1987) The effects of disequilibrium and deformation on the mineralogical evolution of quartz diorite during metamorphism in the eclogite facies. *Journal of Petrology*, **28**, 679–700.
- Krabbendam M. and Wain A. (1997) Late-Caledonian structures, differential retrogression and structural position of (ultra) high-pressure rocks in a Nordjord-Stadlandet area, Western Gneiss Region. *Norges Geologiske Undersøkelse*, **432**, 127–139.
- Krabbendam M., Wain A. and Andersen T.B. (2000) Pre-Caledonian granulite and gabbro enclaves in the Western Gneiss Region, Norway: indications of incomplete transition at high pressure. *Geological Magazine*, **137**, 235–255.
- Kruhl J.H. (1996) Prism- and basal-plane parallel subgrain boundaries in quartz: A microstructural geothermobarometer. *Journal of Metamorphic Geology*, **14**, 581–589.
- Lappin M.A. (1977) Crustal and in situ origin of Norwegian eclogites. *Nature*, **269**(5630), 730–730.
- Lotout C., Pitra P. and Pujol M. (2017) Ordovician magmatism in the Lévézou massif (French Massif Central): tectonic and geodynamic implications. *International Journal of Earth Sciences*, **106**, 501–515.
- Mahar E.M., Baker J.M., Powell R., Holland T.J.B. and Howell N. (1997) The effect of Mn on mineral stability in metapelites. *Journal of Metamorphic Geology*, **15**, 223–238.
- Merlet C. (1994) An accurate computer correction program for quantitative electron probe microanalysis. *Microchimica Acta*, **114**, 363–376.
- Mørk M.B.E. (1985) Incomplete high P–T metamorphic transitions within the Kvamsøy pyroxenite complex, west Norway: a case study of disequilibrium. *Journal of Metamorphic Geology*, **3**, 245–264.
- Mottram C.M., Warren C.J., Regis D., Roberts N.M., Harris N.B., Argles T.W. and Parrish R.R. (2014) Developing an inverted Barrovian sequence; insights from monazite petrochronology. *Earth and Planetary Science Letters*, **403**, 418–431.
- Oberhänsli R., Hunziker J.C., Martinotti G. and Stern W.B. (1985) Geochemistry, geochronology and petrology of Monte Mucrone: An example of Eo-alpine eclogitization of Permian granitoids in the Sesia-Lanzo Zone, Western Alps, Italy. *Chemical Geology: Isotope Geoscience section*, **52**, 165–184.
- Palin R.M., Searle M.P., Waters D.J., Parrish R.R., Roberts N.M.W., Horstwood M.S.A., Yeh M.W., Chung S.L. and Anh T.T. (2013) A geochronological and petrological study of anatectic paragneiss and associated granite dykes from the Day Nui Con Voi metamorphic core complex, North Vietnam: constraints on the timing of metamorphism within the Red River shear zone. *Journal of Metamorphic Geology*, **31**, 359–387.
- Palin R.M., St-Onge M.R., Waters D.J., Searle M.P. and Dyck B. (2014) Phase equilibria modelling of retrograde amphibole and clinozoisite in mafic eclogite from the Tso Morari massif, northwest India: constraining the P – T – M (H₂O) conditions of exhumation. *Journal of Metamorphic Geology*, **32**, 675–693.
- Paquette J.-L., Nédélec A., Moine B. and Rakotondrazafy M. (1994) U-Pb, single zircon Pb-evaporation, and Sm-Nd isotopic study of a granulite domain in SE Madagascar. *The Journal of Geology*, **102**, 523–538.
- Parsons I. and Boyd R. (1971) Distribution of potassium feldspar polymorphs in intrusive sequences. *Mineralogical Magazine*, **38**, 295–311.
- Passchier C.W. and Trouw R.A.J. (2005) Deformation mechanisms. Pp. 25–66 in: *Microtectonics*. Springer-Verlag, Berlin/Heidelberg.
- Peterman E.M., Hacker B.R. and Baxter E.F. (2009) Phase transformations of continental crust during subduction and exhumation: Western Gneiss Region, Norway. *European Journal of Mineralogy*, **21**, 1097–1118.
- Pognante U. and Spencer D. (1991) First report of eclogites from the Himalayan belt, Kaghan valley (northern Pakistan). *European Journal of Mineralogy*, **3**, 613–618.
- Robert J.L. (1976) Titanium solubility in synthetic phlogopite solid solutions. *Chemical Geology*, **17**, 213–227.
- Rubie D.C. (1990) Role of kinetics in the formation and preservation of eclogites. Pp. 111–140 in: *Eclogite Facies Rocks*. Chapman and Hall, UK.

- Sachan H.K., Mukherjee B.K., Ogasawara Y., Maruyama S., Ishida H., Muko A. and Yoshioka N. (2004) Discovery of coesite from Indus Suture Zone (ISZ), Ladakh, India: Evidence for deep subduction, *European Journal of Mineralogy*, **16**, 235–240.
- Scherth H.-P., Schreyer W. and Chopin C. (1991) The pyrope-coesite rocks and their country rocks at Parigi, Dora Maira Massif, Western Alps: detailed petrography, mineral chemistry and PT-path. *Contributions to Mineralogy and Petrology*, **108**, 1–21.
- Shau Y.H., Yang H.Y. and Peacor D.R. (1991) On oriented titanite and rutile inclusions in sagenitic biotite. *American Mineralogist*, **76**, 1205–1217.
- Smith D.C. (1980) A tectonic mélange of foreign eclogites and ultramafites in West Norway. *Nature*, **287**(5780), 366–367.
- Smith D.C. (1984) Coesite in clinopyroxene in the Caledonides and its implications for geodynamics. *Nature*, **310**(5979), 641–644.
- St-Onge M.R., Rayner N., Palin R.M., Searle M.P. and Waters D.J. (2013) Integrated pressure – temperature – time constraints for the Tso Moriri dome (Northwest India): implications for the burial and exhumation path of UHP units in the western Himalaya. *Journal of Metamorphic Geology*, **31**, 469–504.
- Steck A., Epard J.L., Vannay J.C., Hunziker J., Girard M., Morard A. and Robyr M. (1998) Geological transect across the Tso Moriri and Spiti areas: The nappe structures of the Tethys Himalaya. *Eclogae Geologicae Helveticae*, **91**, 103–121.
- Stipp M., Stunitz H., Heilbronner R. and Schmid S.M. (2002) The eastern Tonale fault zone: a natural laboratory for crystal plastic deformation of quartz over a temperature range from 250 to 700 C. *Journal of Structural Geology*, **24**, 1861–1884.
- Swanson S.E. and Fenn P.M. (1986) Quartz crystallization in igneous rocks. *American Mineralogist*, **71**, 331–342.
- Thakur V. and Virdi N. (1979) Lithostratigraphy, structural framework, deformation and metamorphism of the southeastern region of Ladakh, Kashmir Himalaya, India. *Himalayan Geology*, **9**, 63–78.
- Tinkham D.K., Zuluaga C.A. and Stowell H.H. (2001) Metapelite phase equilibria modeling in MnNCKFMASH: the effect of variable Al₂O₃ and MgO/(MgO+FeO) on mineral stability. *Geological Materials Research*, **3**, 1–42.
- Tronnes R.G., Edgar A.D. and Arima M. (1985) A high pressure-high temperature study of TiO₂ solubility in Mg-rich phlogopite: implications to phlogopite chemistry. *Geochimica et Cosmochimica Acta*, **49**, 2323–2329.
- Vance J.A. (1969) On synneusis. *Contributions to Mineralogy and Petrology*, **24**, 7–29.
- Vermeech P. (2018) IsoplotR: a free and open toolbox for geochronology. *Geoscience Frontiers*, **9**, 1479–1493.
- Wain A., Waters D., Jephcoat A. and Olijnyk H. (2000) The high-pressure to ultrahigh-pressure eclogite transition in the Western Gneiss Region, Norway. *European Journal of Mineralogy*, **12**, 667–687.
- Wain A.L., Waters D.J. and Austrheim H. (2001) Metastability of granulites and processes of eclogitisation in the UHP region of western Norway. *Journal of Metamorphic Geology*, **19**, 609–625.
- Wallis S.R., Ishiwatari A., Hirajima T., Ye K., Guo J., Nakamura D., Kato T., Zhai M., Enami M., Cong B. and Banno S. (2007) Occurrence and field relationships of ultrahigh-pressure metagranitoid and coesite eclogite in the Su-Lu terrane, eastern China. *Journal of the Geological Society*, **154**, 45–54.
- Wallis D., Parsons A.J. and Hansen L.N. (2019) Quantifying geometrically necessary dislocations in quartz using HR-EBSD: application to chessboard subgrain boundaries. *Journal of Structural Geology*, **125**, 235–247.
- Warr L.N. (2021) IMA-CNMNC approved mineral symbols. *Mineralogical Magazine*, **85**, 291–320.
- Warren C.J. (2013) Exhumation of (ultra-) high-pressure terranes: concepts and mechanisms. *Solid Earth*, **4**, 75–92.
- White R.W., Powell R., Holland T.J.B. and Worley B.A. (2000) The effect of TiO₂ and Fe₂O₃ on metapelitic assemblages at greenschist and amphibolite facies conditions: mineral equilibria calculations in the system K₂O-FeO-MgO-Al₂O₃-SiO₂-H₂O-TiO₂-Fe₂O₃. *Journal of Metamorphic Geology*, **18**, 497–511.
- White R.W., Pomroy N.E. and Powell R. (2005) An in situ metatextite–diatextite transition in upper amphibolite facies rocks from Broken Hill, Australia. *Journal of Metamorphic Geology*, **23**, 579–602.
- White R.W., Powell R. and Holland T.J.B. (2007) Progress relating to calculation of partial melting equilibria for metapelites. *Journal of Metamorphic Geology*, **25**, 511–527.
- Wickham S.M. (1987) Crustal anatexis and granite petrogenesis during low-pressure regional metamorphism: The Trois Seigneurs Massif, Pyrenees, France. *Journal of Petrology*, **28**, 127–169.
- Wilke F., O'Brien P., Schmidt A. and Ziemann M. (2015) Subduction, peak and multi-stage exhumation metamorphism: Traces from one coesite-bearing eclogite, Tso Moriri, western Himalaya. *Lithos*, **231**, 77–91.
- Young D. and Kylander-Clark A. (2015) Does continental crust transform during eclogite facies metamorphism? *Journal of Metamorphic Geology*, **33**, 331–357.
- Zhang R.Y. and Liou J.G. (1997) Partial transformation of gabbro to coesite-bearing eclogite from Yangkou, the Sulu terrane, eastern China. *Journal of Metamorphic Geology*, **15**, 183–202.
- Zhang R.Y., Liou J.G., Ernst W.G., Coleman R.G., Sobolev N.V. and Shatsky V.S. (1997) Metamorphic evolution of diamond-bearing and associated rocks from the Kokchetav Massif, northern Kazakhstan. *Journal of Metamorphic Geology*, **15**, 479–496.
- Zucali M., Corti L., Roda M., Ortolano G., Visalli R. and Zanoni D. (2021) Quantitative X-ray maps analysis of composition and microstructure of Permian high-temperature relicts in acidic rocks from the Sesia-Lanzo Zone eclogitic continental crust, Western Alps. *Minerals*, **11**, 1421, <https://doi.org/10.3390/min11121421>